ELSEVIER

Tectonophysics 323 (2000) 77–104

TECTONOPHYSICS

www.elsevier.com/locate/tecto

Sedimentary basin deformation: an incremental stress approach

K. Tuncay, A. Park, P. Ortoleva *

Laboratory for Computational Geodynamics, Department of Chemistry, Indiana University, Bloomington, IN 47405, USA

Received 25 January 2000; accepted for publication 14 March 2000

Abstract

A key component of sedimentary basin evolution is the spatial distribution and temporal variation of stress and deformation. The many deformation processes (poroelasticity, fracturing, irreversible nonlinear viscosity, and pressure solution) are inextricably bound in a tightly coupled network which, in turn, is coupled to a myriad of basin diagenetic, thermal and hydrologic processes. In the approach presented here, the various deformation processes are integrated through an incremental stress approach. Together with mass, momentum and energy conservation, this approach yields a complete, fully coupled basin model that captures basin and fault phenomena that are beyond the scope of simpler or decoupled models.

Many of the most interesting basin phenomena are not only dependent on multiple, coupled processes but also are fundamentally three-dimensional. To address this three-dimensional complexity, we have developed a numerical simulator using a moving, adapting, accreting finite element grid which is allowed to deform and to grow and adapt with the addition of sediment to capture smaller sedimentary features.

As a result, our fully coupled, comprehensive model allows one to solve a number of key problems in basin and fault dynamics. These include compaction, fractured reservoir and compartment genesis and dynamics. Examples illustrating these applications are presented for idealized systems and the Piceance Basin (Colorado) and the Permian Basin (West Texas). The incremental stress rheology is found to be a powerful formalism for integrating basin hydrology, diagenesis and mechanics.

Keywords: deformation; rheology; sedimentary basin; stress

1. Introduction

Reconstructing the stress and deformation history of a sedimentary basin is a challenging and important problem in the geosciences and a variety of applications. The latter include petroleum exploration, reserve assessment and production, and earthquake hazard reduction. Progress in this field has been hampered by the absence of an integrated mechanical modeling approach set within the wider context of the coupled reaction, transport and mechanical (RTM) dynamics of a basin. This integration and implementation as a three-dimensional simulator are the major goals of this work.

The strongly coupled nature of the deformation problem may be understood in terms of the feedbacks underlying crustal dynamics. For example, pore fluid pressure affects stress, stress changes can lead to fracturing, and fracturing can affect pore fluid pressure. Similarly, stress can affect mineral solubility, causing mineral dissolution which, in turn, can affect rock rheology and, therefore, stress. Clearly, basin deformation analysis requires accounting of the coupling among the many operating, interacting RTM processes.

* Corresponding author. Fax: +1-812-855-8300.

0040-1951/00/$ - see front matter
PII: S0040-1951(00)00095-0

It has become clear over the past two decades that many geological phenomena can only be explained via strongly coupled RTM models (see reviews in Haase et al. 1980; Ortoleva, 1979, 1990, 1994a; Nicolis and Nicolis, 1987; Ortoleva, et al., 1987a,b; Turcote, 1992). Therefore, modeling sedimentary basin dynamics requires a fully coupled, integrated approach. In the approach presented here, integration is achieved through an incremental stress (Zienkiewicz and Cormeau, 1974; Rice, 1975) approach.

The goal of the modeling presented here is to calculate the evolution of the distribution within a basin of the set of descriptive variables characterizing its internal state:

- rock texture and mineralogy
- fluid properties
- temperature
- rock deformation
- fracture network characteristics
- stress.

These properties respond over geological time to their interactions among each other and via the influence of the basin's surroundings. These features are summarized in Fig. 1. The interaction with the surroundings provides the boundary conditions to which the equations of mass, energy and momentum conservation must be subjected to arrive at the evolution of the basin. In this way, basin analysis becomes the delineation of the RTM basin dynamical system and its response to the constraints imposed at the boundaries. As the laws for the basin RTM processes are nonlinear in the descriptive variables, one expects this response to be extremely rich (Ortoleva, 1993, 1994a,c, 1998; Dewers and Ortoleva, 1994).

Other models do exist and have been used to gain valuable insights into the basin system.

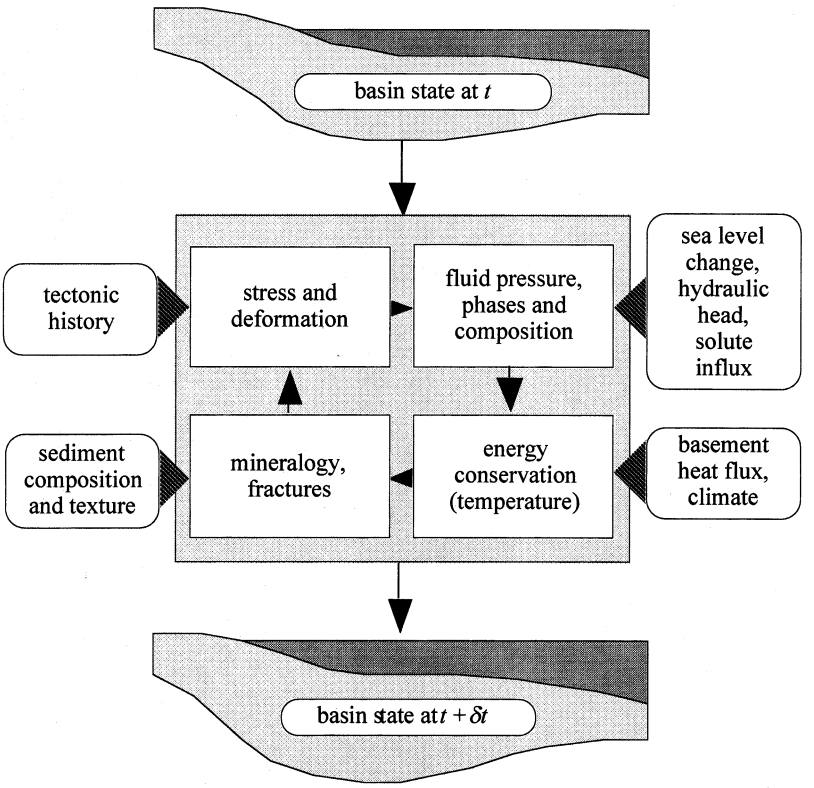

Fig. 1. Flow chart showing how the interplay of geologic data and physico-chemical (i.e., reaction–transport–mechanical) process modules evolve the basin over a computational time interval δt.

However, the many strongly coupled basin RTM processes as suggested in Fig. 1 require a comprehensiveness and three-dimensional approach that goes far beyond these two- or three-process, typically two-dimensional models (Ungerer et al., 1990; Larson et al., 1993; Maubeuge and Lerche, 1993, 1994; Dewers and Ortoleva, 1994; Sonnenthal and Ortoleva, 1994; Roberts and Nunn, 1995; Luo and Vasseur, 1996; Schneider et al., 1996; Luo et al., 1998; Wang and Xie, 1998). To be effective, models must be fully three-dimensional to capture basin sedimentological geometry, fracture orientation, changing compression/extensional tectonic regimes and basement heat flux anomalies.

Fracture mediated petroleum migrations from reservoirs are key aspects of the dynamic petroleum (or other crustal fluid) system. In most of the existing basin evolution models, it is assumed that rocks fracture when the fluid pressure exceeds a certain fraction of lithostatic stress (Ghaith et al., 1990; Maubeuge and Lerche, 1993, 1994; Chen et al., 1994; Sonnenthal and Ortoleva, 1994; Roberts and Nunn, 1995; Wang and Xie, 1998). This assumption essentially eliminates the dependence of fracturing on lithologic properties. In this study, we find that fracturing strongly depends on the rock texture, i.e., mineral composition, grain size, porosity, etc. For example, the difference in neighboring sandstone and shales with respect to their fracture response is commonly observed (Kulander et al., 1979; Segall and Pollard, 1983; Hancock et al., 1984; Lorenz et al., 1991; Gross, 1993; Fischer et al., 1995; Wu and Pollard, 1995; Payne et al., 2000). Although fracturing can occur in almost any type of rock, they are more common in brittle rocks (Mallory, 1977). Furthermore, fractures in a brittle lithology commonly discontinue at the interface of more ductile lithologies (Engelder and Geiser, 1980). Another observation is that fracture spacing is strongly dependent on bed thickness and lithology (Harris et al., 1960; Nickelsen and Hough, 1967; Gross, 1993; Fischer et al., 1995; Wu and Pollard, 1995).

Another limiting assumption made in other studies is that there exists a simple dependence of porosity on effective stress (Ungerer et al., 1990; Maubeuge and Lerche, 1993, 1994; Roberts and Nunn, 1995; Luo and Vasseur, 1996; Schneider et al., 1996; Wang and Xie, 1998). This results in a very smooth porosity profile and, once again, eliminates the importance of the lithologic dependence of rock properties. In our approach, porosity is obtained by solving the mass conservation equation for the solids using the rock deformation velocity computed by a multi-process, incremental stress rheology. Since, in our approach, the elastic, viscous and yield parameters are functions of texture, the evolution of porosity and stress are strongly coupled and thereby computed self-consistently. As a result, shales tend to have lower porosity and higher least-compressive stress than sandstones. The small grain size combined with low porosity results in very low permeability and, thus, these layers can form efficient seals. Furthermore, our results show that low shear viscosity/bulk viscosity ratio makes fracturing very unlikely in the absence of flexure or extreme overpressuring. Mechanisms of overpressuring include petroleum generation, fluid thermal expansion and compaction. In the numerical results presented here, we illustrate the episodic fracturing of a seal layer resulting from a high rate oil generation.

In other basin evolution simulators, fracture permeability is assumed to be isotropic. This can be attributed to the fact that, for an accurate description of fracture orientations, the full stress tensor must be known. In our approach, a representative set of putative fractures of a range of orientations is introduced. The time dependent properties of each realized fracture are calculated by using the stress component normal to its fracture plane, pressure and rock properties. The anisotropic fracture permeability is obtained using the predicted fracture network statistics (see Tuncay et al., 2000 for details).

Another effect that is always disregarded is the volumetric strain caused by fracturing. As fractures open, the overall rock volume increases and fluid pressure decreases (due to flow and increase in pore volume). This reduces the rate of fracture growth. Therefore, fracturing is a self-limiting process. In summary, a fully coupled deformation/hydrologic/fracturing model is required to capture the co-evolution of these fracture enhancing and limiting factors.

Although one- and two-dimensional studies give

hints into the dynamics of basin evolution, a three-dimensional basin simulator is necessary to take into account all geometric effects. This becomes extremely important when fracturing is due mainly to flexure and the direction of tectonic compressive/extension is changing over the basin's history. Fracture networks provide a pathway for fluid flow and, especially in a layered medium, fluids can move laterally. This can only be taken into account by a three-dimensional basin simulator with a stress/deformation solver that can capture the nonplanar layers (notably domes) and the strong variations in rheology from layer to layer (e.g., sandstones versus shales or salt). The fundamentally three-dimensional nature of these systems is further enhanced as preferred fracture orientation induces anisotropic permeability tensor that can strongly influence the direction of fluid flow. To our knowledge, existing basin evolution simulators are mostly one- or two-dimensional (Ungerer et al., 1990; Larson et al., 1993; Maubeuge and Lerche, 1993; 1994; Roberts and Nunn, 1995; Luo and Vasseur, 1996; Schneider et al., 1996; Luo et al., 1998; Wang and Xie, 1998).

Although the history of basement heat flux, sedimentation and erosion rates, and subsidence and upheaval rates are among the most important parameters that effect the basin evolution, some basin simulators start with a predefined grid (Schneider et al., 1996). In other words, two basins with the same final thickness and sediments but different histories are assumed to behave similarly. It is well known that overpressuring, a key factor in fracturing and other deformation processes, correlates with sedimentation rate (Dewers and Ortoleva, 1994; Wang and Xie, 1998; Ortoleva, 1998).

In the classical flexure analysis, the history of deformation and its relation to the lithologic properties is ignored although present-day flexure is often a poor indication of fracturing. If the rate of flexure development was very slow, then rocks could have deformed continuously, depending on viscosities, and there would be no fracturing. Flexure can occur without fracturing early in a sediment's evolution, i.e., when it is poorly lithified or if it has inherently ductile behavior (as for organic-rich shales, rock salt or anhydrates). Therefore, the next generation of basin evolution simulators should be not only three-dimensional, but should also consider the history of sedimentation, erosion, tectonic and thermal evolution and their interplay with deformation.

2. Modeling concept

The conservation laws are universal; it is the differences in the history of the evolving boundary conditions that give a basin its individual character. Thus, one might state that the geology is in the boundary conditions and the physics and chemistry imply the form of the conservation equations.

In this study, we attempt to demonstrate that the integration of mechanics into a basin RTM model can be done most effectively using an incremental stress approach (Ortoleva, 1994a, 1998). In analogy with the classic theory of chemical kinetics, the total rate of strain ϵ is written as a sum of terms, each accounting for a particular process ($j=1,2,\ldots N_d$) for a system with N_d deformation processes:

$$\dot{\underline{\underline{\epsilon}}} = \sum_{j=1}^{N_d} \dot{\underline{\underline{\epsilon}}}^{(j)}. \tag{1}$$

Such processes included in this study are:

- poroelasticity
- continuous, irreversible rock deformation
- fracturing
- pressure solution

Recently, we have studied contributions of gouge, and coal devolitilization shrinkage/cleating to the total rate of strain (Ortoleva, 1998; Ozkan et al., 1998; Ozkan and Ortoleva, 1999b). Each of the deformation processes includes a variety of possibilities. For example, fracturing may be induced by flexure or elevated fluid pressure. Devolitilization in coals, dehydration, and thermally-induced shrinkage may also lead to fractures.

The outstanding contribution of incremental stress theory is that the total rate of strain is expressible as a linear combination of rate of strains from different process due to the fact that it represents a relation among infinitesimal changes. Multiplying both sides of Eq. (1) by a

small time increment dt, the equation states that an infinitesimal deformation is expressed as a sum of infinitesimal deformation due to various processes. This type of statement has been the basis of chemical kinetics over the past century and has entered in fundamental physics at least as far back as Newton who recognized that the rate of change of momentum was equal to a linear combination of forces.

The individual rate of strain terms on the right-hand side of Eq. (1) depend on the full suite of rock textural and fluid properties as well as the macroscopic stress. It is through this dependence and the coevolution of rock deformation and of these variables that the full coupling of all processes is accounted for in our model. As the rates $\underline{\underline{\dot{\varepsilon}}}^{(j)}$ typically vary stronger than linearly with these variables, the basin is a nonlinear dynamical system.

We suggest that rigorous models of rock behavior should be of the Morkov type – i.e., the rate of change of rock state should only depend on the instantaneous rock state and not on prior history. Stress and strain are related through rock rheology, to rock texture Θ (grain size, shape, packing, mineralogy, and fracture length, aperture and orientation statistics). Pressure solution and grain breakage imply that the rate of change of Θ depends on stress, denoted σ. If Θ satisfies the different equation $d\Theta/dt = G(\Theta,\sigma)$ then, in principle, $\Theta(t)$ is a functional of σ, i.e., depends on $\sigma(t' < t$, i.e., the stress history: $\Theta = \Theta[\sigma]$. As rheology depends on Θ we see that $\Theta[\sigma]$ reflects the entire prior stress history and not just the instantaneous value of σ. Clearly, however, this "memory" in a theory wherein Θ is not coevolved with σ is an artefact of the incompleteness of a rock deformation model that attempts to avoid coevolving Θ with stress. While there are many stress–strain histories that could lead to the instantaneous state of a rock, only the latter is key to predicting its failure and other behavior.

Our model uniquely accounts for the changing rock rheological parameters that accompany the changing texture (e.g., grain size, mineralogy and porosity) and fracture network properties (length, aperture, number density and orientation statistics). The bulk, shear and effective stress coefficients of the (assumed) isotropic rocks are computed using Berryman's composite medium theory (Berryman, 1980, 1986, 1992). The shear and bulk viscosities are assumed to depend on grain contact areas and mineralogy, fitting specific formulae to geologic and experimental data from a series of test basins. Thus, the mechanical and diagenetic modifications of texture directly affect rheology which, then, is used to compute basin stress/deformation history using our extended incremental stress rheology.

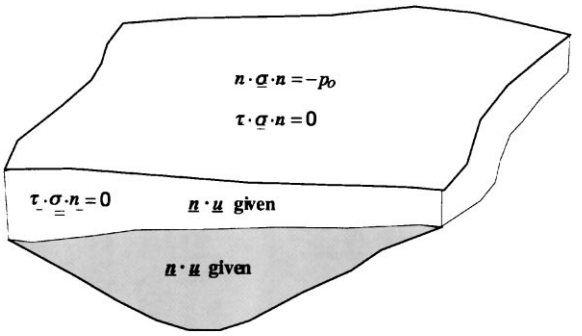

Fig. 2. Conditions at the boundary of basin simulation domain allow for imposition of ocean bottom normal pressure p_o and no shear at the top ($\underline{\tau}$ being a unit tangent vector and $\underline{n}$ being an outward pointing unit normal vector with respect to the basin boundary). At the bottom, the tectonic history fixes the evolution of the deformation velocity $\underline{u}$ using slip conditions as on the sides lightly shaded). The normal velocity $\underline{n}\cdot\underline{u}$ is imposed by the prescribed history of upheaval/subsidence and compression/extension.

The particular boundary conditions that are used to completely pose the rheologic problem are illustrated in Fig. 2. These conditions enforce the lateral compression/extension and subsidence/upheaval imposed by the larger-scale tectonics. The interaction of the top of the sediment pile with the overlying fluids (atmosphere or sea bottom) is accounted for by the value of normal stress and the (assumed) absence of tangential shear. The no vertical-shear lateral boundary condition allows for natural compaction at the sides of the basin.

Nonlinearity and coupling are key reasons for constructing a comprehensive basin model. The modern theory of nonlinear dynamical systems has revealed their great potential for supporting a host of phenomena that arise autonomously, i.e., with-

out their imposition by an external template. Nonlinear systems can, for example, oscillate periodically or chaotically in time and may organize spatially in regular spatial patterns (see Ortoleva, 1987a, 1987b, 1990, 1994a; Nicolis and Nicolis, 1987; Turcote, 1992).

A necessary condition that such autonomous spatio-temporal organization can take place is that the system be maintained sufficiently far from equilibrium (Nicolis and Prigogine, 1977). The potential importance of nonlinear dynamics in geological systems has been the subject of several conferences (Nicolis and Nicolis, 1987; Ortoleva et al., 1990a) and has been investigated extensively in the context of geochemistry (Ortoleva, 1994a). For the sedimentary basin, it has been pointed out (Ortoleva, 1993, 1994a,b,c; Maxwell, 1997) that nonlinear dynamics can play an important role on a wide range of spatial scales. This potential autonomy of behavior suggests that many patterns of mineralization, petroleum reservoirs, fault motion and other phenomena cannot be understood as direct consequences of related patterns of sedimentology, volcanism or tectonism, i.e., cannot be attributed to an external template. Owing to the large network of processes underlying basin dynamics, as well as the nonlinearity of the conservation equations, a computational modeling approach is likely the only way to delineate nonlinear basin phenomena and the range of conditions (overall tectonics, sedimentation history, etc.) for which they occur.

Far-from-equilibrium conditions, necessary for the operation of autonomous spatio-temporal patterning, can be obtained in a sedimentary basin. The basin is sustained out of equilibrium by the fluxes and forces applied to the boundary of the basin. Input of sediment presents the basin with minerals and fluid chemical species which, after burial, are out of equilibrium at the local pressure and temperature or other conditions. Changes in tectonic forces, heat flux or influxed magmatic or meteoric fluids can also cause all or part of the basin to be driven out of equilibrium. Other factors are the drive of the overburden towards compaction and buoyancy drive of low density fluids (oil, gas or hot aqueous liquid) to rise. These factors that drive the basin out of equilibrium are directly or indirectly imposed at the basin boundaries. Thus, as suggested in Fig. 2, the conditions inducing change within a basin are expressed in terms of the boundary conditions imposed on the solution of the conservation equations. Clearly, rapid burial, large geothermal gradients or large amounts of chemically unstable kerogen are examples of factors favoring an increase in the likelihood of autonomous basin behavior. The comprehensive, three-dimensional, fully coupled model presented here is designed to capture this richness in autonomous basin behavior.

In this study, we use the updated Lagrangian approach to analyze the time dependent large deformation behavior of geological materials with the incremental stress rheologic behavior (Bathe et al., 1975; Synder and Bathe, 1981; Bathe, 1996). In our numerical approach, all variables are referred to an updated configuration in each time step. The approach has two major steps. First, the incremental stress rheology is solved at the integration points of the finite elements. Second, the displacements are computed by using a global deformation solver. Iterations of these two steps are performed until the norm of the change in displacements between two consecutive iterations is less than a specific tolerance. The two-step solution technique allows the introduction of new deformation mechanisms with only minor changes in the code.

The finite element grid accretes with sediment infilling. A new sediment layer is introduced when the sediment layer at the top of the basin reaches a critical thickness. In contrast, when erosion creates a top layer that is locally too thin, the finite element grid is locally reorganized to preserve numerical accuracy. This accreting, reorganizing grid that also adapts to sedimentary features as they are added (i.e., to capture thin beds) is required to capture sedimentary detail and ensure numerical stability and accuracy.

We use the conjugate gradient iterative technique with simple diagonal preconditioner to solve for the incremental displacements. The finite element code and iterative solver are parallelized.

In the following sections, the incremental stress rheology is introduced. Then, the explicit formulation of the rate of strain is provided for poroelasticity, irreversible nonlinear viscosity, pressure solution, and fracturing. The numerical solution technique

and finite element formulation are provided in the Appendix. One- and three-dimensional simulations of the Piceance Basin (Colorado) and the Andector Field, Permian Basin (West Texas) are used to illustrate the capabilities of our approach.

3. Incremental stress rheology

The strongly coupled nature of the basin deformation problem is captured using an incremental stress rheology. Let us make some of the coupling explicit. The poroelasticity rate of strain $\dot{\underline{\underline{\epsilon}}}^{(pe)}$) may be expressed in terms of total stress $\underline{\underline{\sigma}}$, wetting phase fluid pressure p, and rock texture Θ via:

$$\dot{\underline{\underline{\epsilon}}}^{(pe)} = \underline{\underline{D}}^{-1}(\Theta)\,\frac{D}{Dt}\,(\underline{\underline{\sigma}} + \alpha(\Theta) p \underline{\underline{I}}) \tag{2}$$

for fourth rank tensor of poroelastic coefficients $\underline{\underline{D}}$ and effective stress coefficient α; D/Dt represents a material time derivative measuring the rate of change of a tensor in time with respect to a local reference frame fixed to a translation, rotating material point. The texture Θ represents a set of variables characterizing the mineralogy, shape, size, orientation, and packing of the grains, and also the fracture length, aperture, number density and orientation statistics. In summary:

$$\dot{\underline{\underline{\epsilon}}}^{(pe)} = \dot{\underline{\underline{\epsilon}}}^{(pe)}(\Theta, p, \underline{\underline{\sigma}}), \tag{3}$$

illustrates the strong coupling among deformation, fluid properties and texture.

A direct coupling of mechanics and chemistry arises through pressure solution. Grain dissolution at stressed grain–grain contacts induces compaction and thereby contributes to $\dot{\underline{\underline{\epsilon}}}$. The rate of this pressure solution contribution, $\dot{\underline{\underline{\epsilon}}}^{(ps)}$, depends on the stress at grain–grain contacts and, hence, on the macro-stress $\underline{\underline{\sigma}}$, fluid pressure and texture. However, $\dot{\underline{\underline{\epsilon}}}^{(ps)}$ should also depend on the composition of the pore fluid. The latter may be characterized by the set of concentrations $c = \{c_1, c_2, \ldots c_N\}$ for the N pore fluid species system; hence $\dot{\underline{\underline{\epsilon}}}^{(ps)}$ depends on $\underline{\underline{\sigma}}$, Θ, p and c.

As the present theory is macroscopic, the variables describing fractures (length, aperture, number density and orientation statistics) are considered to be part of the texture Θ (Tuncay et al., 2000). This assumes that the length scale on which the phenomena of interest vary is much greater than the fracture length or inter-fracture spacing. Otherwise one must treat fractures individually, an approach that is not viable for basin-scale modeling. With our macro-textural description, one must allow for the potential influence of the fracture variables on rock mechanical and other properties.

One expects that $\dot{\underline{\underline{\epsilon}}}^{(j)}$ (where j = poroelasticity, viscosity, pressure solution, fracturing, etc.) should, in general, depend on all the aforementioned variables $(\underline{\underline{\sigma}}, \Theta, p, c)$, as well as absolute temperature T. With this:

$$\dot{\underline{\underline{\epsilon}}} = \sum_{j=1}^{N_d} \dot{\underline{\underline{\epsilon}}}^{(j)}(\Theta, \underline{\underline{\sigma}}, p, c, T) \tag{4}$$

The dependency of $\dot{\underline{\underline{\epsilon}}}^{(j)}$ on the indicated state variables may be nonlocal in time. For example, in the case of poroelasticity, $\dot{\underline{\underline{\epsilon}}}^{(pe)}$ depends on the time-derivative of effective stress (see Eq. (2)). Therefore, the $\dot{\underline{\underline{\epsilon}}}^{(j)}$ may be functionals of their arguments that can, in principle, sample the state variables in some finite volume of space–time.

The total rate of strain $\dot{\underline{\underline{\epsilon}}}$ is defined by:

$$\dot{\epsilon}_{ii'} = \frac{1}{2}\left(\frac{\partial u_i}{\partial x_{i'}} + \frac{\partial u_{i'}}{\partial x_i}\right). \tag{5}$$

The six independent components of the symmetric second rank tensor Eq. (4) must be supplemented with three additional equations so that the three deformation velocity components $(\underline{u} = u_1, u_2, u_3)$ can be determined. The required condition arises from force balance:

$$\sum_{i'=1}^{3} \frac{\partial \sigma_{ii'}}{\partial x_{i'}} + f_i = 0 \tag{6}$$

for body force f_i which, for gravity, is given by:

$$f_i = g \rho_m \delta_{i3}. \tag{7}$$

Here g is the gravitational acceleration, ρ_m is the mass density, and the 3-direction is upward.

The above formulation must be augmented with equations of texture dynamics and fluid mass and energy conservation (the latter to fix T). With this, the model provides a complete theory of basin dynamics when the equations are solved using the

boundary conditions imposed by the overall tectonics and by the surfacial fluids (i.e., ocean bottom and atmospheric pressure) (Figs. 1, 2).

Effects such as strain hardening or weakening are accounted for in the present model via the coupled dynamics of texture and stress. The differential equations of texture evolution introduced the time delays (memory) that make our rheology capture hardening or softening. The latter properties are reflections of texture, i.e., hardness/weakness is a unique function of texture but not of stress. Thus, rock rheology depends on texture which, via the evolution equations of the latter, depends on the history of deformation.

To complete the incremental stress formulation, explicit expressions for the rate functions $\underline{\underline{\dot{\epsilon}}}^{(j)}(\Theta,\underline{\underline{\sigma}},p,c,T)$ are required. For $\underline{\underline{\dot{\epsilon}}}^{(ps)}$, for example, these can be obtained through geometric considerations of the texture variables and the rate of grain shortening from pressure solution (see Dewers and Ortoleva, 1994 and Ortoleva, 1994a, 1998).

The dependence of the strain rates on state clarifies the central role of incremental stress theory in integrating all the RTM basin processes into a unified model. It is the coupling allowed by this integration that underlies many key basin phenomena from fault dynamics to episodic fluid flow, seal formation and overpressure.

In addition to the coupling of deformation to other phenomena through the incremental stress formulation, there are numerous indirect couplings. For example, rock properties such as permeabilities, reactive grain surface area and thermal conductivities depend strongly on texture. As the latter is affected by stress and deformation, a complex network of coupling relations is thereby expressed. For further discussion of the consequence of this network, see Ortoleva et al. (1987a, 1987b), Ortoleva (1994a, 1994b, 1994c, 1998), and Dewers and Ortoleva (1994).

4. Explicit formulation of the $\underline{\underline{\epsilon}}^{(j)}$

4.1. Poroelasticity

The poroelastic formulation adopted is as in Eq. (2). It is the implementation of the theory of Biot (Biot, 1941; Gassman, 1951; Biot and Willis, 1957) modified for an incremental strain rate. When the medium is isotropic, the fourth rank elasticity tensor can be written as:

$$D_{ijkl} = K\delta_{ij}\delta_{kl} + G(\delta_{ik}\delta_{jl} + \delta_{il}\delta_{jk} - \tfrac{2}{3}\,\delta_{ij}\delta_{kl}) \qquad (8)$$

where K and G are bulk and shear moduli of the drained porous medium. These moduli and the effective stress coefficient of the macroscopic porous medium can be approximately calculated in terms of the grain sizes, composition, porosity, and mineral elastic properties by using Berryman's (1980, 1986) approach.

4.2. Nonlinear viscosity and yield

The inelastic mechanical contribution to $\underline{\underline{\dot{\epsilon}}}$ is cast in the present approach as a nonlinear viscosity law in the form:

$$\underline{\underline{\dot{\epsilon}}}^{(vp)} = \underline{\underline{\eta}}^{-1}(\underline{\underline{\sigma}} + \tilde{\alpha}p\underline{\underline{I}}). \qquad (9)$$

The fourth rank viscosity tensor $\underline{\underline{\eta}}$ depends on stress, fluid pressure and texture. The second term in the effective stress involves a coefficient $\tilde{\alpha}$ that is usually taken to be unity. The viscosity tensor is assumed to be isotropic:

$$\eta_{ijkl} = \kappa\delta_{ij}\delta_{kl} + \mu(\delta_{ik}\delta_{jl} + \delta_{il}\delta_{jk} - \tfrac{2}{3}\,\delta_{ij}\delta_{kl}) \qquad (10)$$

for shear and bulk viscosities μ and κ, respectively. To capture faulting, shear viscosity is assumed to depend on a yield function F. In the present work, we adopt the transitional form:

$$\frac{1}{\mu} = \frac{1}{\mu_-} + \left[\frac{1}{\mu_+} - \frac{1}{\mu_-}\right]\frac{1}{1+\exp[-(F+w)/\Delta]} \qquad (11)$$

where μ_- and μ_+ are the viscosities before ($F<0$) and after ($F>0$) yield, respectively, and $w=\Delta\ln(\mu_-/\mu_+)$ such that $\mu=0.5(\mu_-+\mu_+)$ for $F=0$. The width of the yield transition Δ, like κ, μ_+ and μ_-, depends on Θ (and possibly on other state variables, notably $\underline{\underline{\sigma}}$, p, T and c).

The texture dependence of the viscosities is not

well characterized. We conjecture that the area of grain–grain contact should strongly affect the viscosities. Assume that the greater the free face area relative to grain–grain contact area, the lower the viscosity. For a monomineralic system, let x_f be the fraction of a grain surface that is free (and not in contact with other grains). Then consider the assumption:

$$\mu_{-} = \mu_{-}^{0} \frac{1 - x_f/x_f^*}{1 + \left(x_f/x_f^0 \right)^{\gamma}} \tag{12}$$

for parameters x_f^*, x_f^0, and μ_{-}^{0} that are particular for each mineral. Note μ_{-}^{0} is the viscosity for the zero porosity, monomineralic rock. An alternative approach is the approximation of viscosities as a function of grain size and porosity. For example:

$$\mu_{-} = A \exp(-\phi/B\phi^0)^n g(r) \tag{13}$$

where A, B, and n are material properties, $g(r)$ is a correction for grain size r, and ϕ is porosity.

For the M mineral system ($i = 1,2,\ldots M$), consider the mode (solid volume fraction) average:

$$\eta_{-}^{-1} = \frac{1}{1-\phi} \sum_{i=1}^{M} \phi_i \eta_{-i}^{-1} \tag{14}$$

Here η_{-i} is η_{-} for a pure mineral i rock and ϕ_i is the fraction of rock volume occupied by mineral i. Note that:

$$1 - \phi = \sum_{i=1}^{M} \phi_i.$$

The yield function F is assumed to take the form (Drucker-Prager and Prager, 1952):

$$F = aJ_1 + b\sqrt{J_2} - c \tag{15}$$

where J_1 is the first invariant of the effective stress tensor and J_2 is the second invariant of the deviatoric effective stress tensor. The dependence of the a, b, c coefficients on mineralogy and texture has been fit with experimental data (Ozkan and Ortoleva, 1999a).

4.3. Pressure solution

Attempting to formulate an expression for the contribution to $\underline{\underline{\dot{\epsilon}}}$ due to pressure solution requires a careful delineation of the grain-scale deformation processes. These include:

- dissolution at grain–grain contacts;
- granulation at grain–grain contacts;
- grain boundary slip;
- plastic deformation of single grains; and
- grain breakage.

In general, several or all of these microscopic processes are acting simultaneously and may be strongly interacting. It thus may be appropriate to further refine our incremental stress rheology such that $\underline{\underline{\dot{\epsilon}}}^{(vp)} + \underline{\underline{\dot{\epsilon}}}^{(ps)}$ is written as a sum of the aforementioned processes. In the present work, we shall limit our treatment to only include an explicit accounting of pressure solution via simple texture geometric models wherein the geometry of packing does not change its character due to nonpressure solution processes and all the other irreversible processes are assumed to be captured by $\underline{\underline{\dot{\epsilon}}}^{(vp)}$ as introduced above. Limitations to such a model include the neglect of gouge and a lack of a clearly defined accounting of the other nonpressure solution processes. Progress in the development of more refined models will be the subject of other studies.

Pressure solution-derived rates of strain must be formulated through a relation between the rate of change of variables characterizing the texture and through the geometric relation between texture and macroscopic strain. Such formulations have been presented elsewhere for simple texture models (Ortoleva, 1998). Their model does account for some of the interplay of mechanical and pressure solution deformation by allowing grain geometry and packing to depend on porosity, the latter being the aggregate effect of all strain processes.

The simplest pressure solution models are isogeometric. For them, the symmetry of grain packing is assumed to be preserved as pressure solution tends to dissolve minerals at grain–grain contacts that bear normal stress in excess of fluid pressure. For a single stress-supporting mineral system considered to be a periodic array of truncated spheres,

the formula (Dewers and Ortoleva, 1990, 1994):

$$\epsilon_{33}^{(ps)} = \frac{G_3}{L_3} \tag{16}$$

was used, where G_3 is the rate of grain shortening in the vertical (3) direction from pressure solution and L_3 is the grain height. In that formulation, the grains are described in terms of L_3, two horizontal truncation lengths L_1 and L_2, and the sphere radius L_4. Porosity can be expressed in terms of the L values. The rate G_3 depends on the normal stress P_3 to the horizontal grain–grain contacts. To obtain a complete theory, this quantity must be related to the macroscopic stress $\underline{\underline{\sigma}}$ operating on a volume element containing many grains and on the texture $\Theta = \{L_1, L_2, L_3, L_4\}$. This relation has been taken to be in terms of the surface area average:

$$L_1 L_2 \sigma_{33} = -A_3 P_3 - (L_1 L_2 - A_3) p \tag{17}$$

for grain–grain contact area $A_3(\Theta)$ and fluid pressure p. This formalism has been generalized to multi-mineralic problems and for random arrays of grains of a range of sizes and shapes (Ortoleva, 1998).

Chemistry enters the pressure solution rate law through the stoichiometry of the mineral dissolution reaction and the pore fluid composition $c(=\{c_1, c_2, \ldots c_N\})$ of the N pore fluid species in the (assumed) single fluid phase. In the case of quartz, it is found to good approximation that:

$$\frac{DL_3}{Dt} = G_3 = k_3 [c_{SiO_2(aq)} - K(P_3)] \tag{18}$$

for material derivative D/Dt, rate coefficient k_3 and equilibrium constant K. The latter increases with p_2 due to variations of free energy with normal stress. More complex dependencies of K on stress have also been considered when strain energy is taken into account. The rate coefficient k_3 depends on the properties of the water film within the grain–grain contact and, thereby, can also depend on P_3, p, and, in principle, c (Renard et al., 1997, 1999). All the above quantities depend on temperature T, coupling the equation of mechanics, pore fluid chemistry, and hydrology to that of energy transport. In the simulations presented below, the approaches of Renard et al. (1997, 1999) are used.

4.4. Fractures

We have developed a model of the probability for fracture length, aperture and orientation (Tuncay et al., 2000). The model predicts the evolution of this probability in response to the changing stress, fluid pressure, and rock properties as the basin changes. The fracture probability is used to compute the permeability tensor. The latter affects the direction of petroleum migration; information which is key to finding new resources. It is central to planning infill drilling spacing and likely directions for field extension. It is key to the design of horizontal wells and the optimum rate of production in stress-sensitive reservoirs. Finally, the predicted distribution of fracture network statistics across a field is a necessary input to reservoir simulators used to optimize production.

The dynamics of the fracture network in our model is based on a statistical representation. For example, consider a set of fractures of length L with normal $\underline{n}$ for a three-dimensional spectrum of normal orientations. Then the rate of change for L in the rock-fixed frame takes the form:

$$\frac{dL}{dt} = R(p, \Theta, \underline{\underline{\sigma}}) \tag{19}$$

where the fracture extension rate R depends on the normal stress σ, the wetting phase fluid pressure p and the texture Θ of the surrounding rock (including fracture length and aperture). A similar equation for the fracture aperture is developed (see Tuncay et al., 2000 for further details).

Let f' be the number density of sites at which fractures may nucleate. By definition of the undeformed state, $f' = f$ but f' can differ from f due to changes in rock texture from diagenesis or mechanical processes. In the simplest case where fracture nucleation sites are not created or destroyed, f' obeys the conservation equation $\partial f'/\partial t + \underline{\nabla}.(f'\underline{u}) = 0$. In a macrovolume element of volume V there are Vf' fracture nuclei and hence a fracture void space $Vf'\pi r^2 a$ where a and r are the aperture and radius of the assumed penny-shaped fractures,

respectively. To compute the dilatation, we focus on a fixed volume V_m of solids and follow its change in a time δt. The volume of the unfractured rock V_{unfr} is related to V_m and the porosity ϕ_m of the unfractured rock via $V_{unfr}=V_m+\phi_m V_{unfr}$. Hence, $V_{unfr}=V_m/(1-\phi_m)$. Note that total porosity is equal to $\phi=\phi_m-\phi_{fr}$. The total volume V of the sample of rock containing V_m is then

$$V=(1-\phi_m)^{-1}V_m+V\Delta \tag{20}$$

where $\Delta=f'\pi L^2 a$. With this, the volume of rock $V(t)$ at time t for fixed volume of solids V_m (considered incompressible and not to expand thermally or react) is given by

$$V(t)=V_m(1-\phi_m)^{-1}(1-\Delta). \tag{21}$$

Noting that

$$tr\underline{\underline{\dot{\epsilon}}}^{(fr)}=\lim_{\delta t\to 0}\frac{V(t+\delta t)-V(t)}{V(t)\delta t} \tag{22}$$

one obtains

$$tr\underline{\underline{\dot{\epsilon}}}^{(fr)}=[1-\Delta]^{-1}\frac{D\Delta}{Dt} \tag{23}$$

where D/Dt is the material derivative, i.e., the derivative in the reference frame fixed to the solids.

The tensor character of the fracture-mediated deformation is related to the directions of each fracture through its normal $\underline{n}$ to the fracture plane. Consider the expression

$$\dot{\epsilon}_{kl}^{(fr)}=[1-\Delta]^{-1}\frac{D}{Dt}(\Delta n_k n_l). \tag{24}$$

Here D/Dt represents a material time derivative; however, now, it must also account for the rotation of the fracture normals as they change direction with flexure, shearing or other deformation. Note that the trace of this expression agrees with the earlier result for the dilatation. Finally, this expression agrees with simple cases wherein all fractures are parallel.

In our model, a finite (but representative) number of fracture orientations is accounted for. We use the fracture kinetics formulation of Ortoleva (1994a), and Sonnenthal and Ortoleva (1994). However, here we replace the least compressive stress in the formulation by the stress component normal to each fracture plane. This allows calculation of fracture length and aperture for each fracture orientation. For example, if we assume that only vertical fractures can occur as for a one-dimensional problem, since the stress component normal to any vertical plane is the same because of the symmetry, an isotropic fracture network develops. In three-dimensional problems, our proposed algorithm has the power to predict a complex fracture network with preferential orientations dictated by the structure of the stress tensor.

Since the fracture network is well defined, the anisotropic fracture permeability can be calculated approximately. The anisotropic fracture permeability of a fracture network consisting of a single fracture orientation is given by

$$K_{ij}^{fr}=\lambda(\delta_{ij}-n_i n_j) \tag{25}$$

where $\underline{n}$ is the unit normal to the fracture plane and K^{fr} is the fracture permeability. The parameter λ can be approximated by

$$\lambda=\beta\phi_{fr}\frac{a^2}{12}. \tag{26}$$

Here β is a factor accounting for the connectivity of fractures. For large fracture lengths and dense networks β approaches unity whereas for small fracture lengths and low fracture densities it vanishes (Oda, 1986). Oda (1985, 1986) proposed that this coefficient should be a function of a dimensionless second order tensor of fracture geometry. He called this tensor the fabric tensor (Oda, 1982). A discussion of this factor can be found in later papers by Oda (1985, 1986). In this study, β is taken as unity. We assume that the total fracture permeability is obtained by summation of fracture permeabilities for all orientations and statistical classes multiplied by the fracture porosity which has been proposed previously by Chen et al. (1999). It is assumed that fluid flow is slow and the disturbance at fracture intersections is negligible. Summation is inadequate when the fracture density is lower than the percolation threshold

(Odling, 1992; Berkowitz, 1995; Bour and Davy, 1998). Another limitation is due to the surface roughness of fractures. In this study, fracture aperture is assumed to be constant in a particular fracture. The spatial distribution of fracture aperture alters the fracture permeability. Waite et al. (1998) measured water flow through a sinusoidal fracture to compare sinusoidal flow with parallel plate flow. Their experimental and numerical results showed that a sinusoidal fracture has a significantly lower permeability and for the sinusoidal geometry the effective aperture is very close to the minimum value of the normal aperture. Thomson and Brown (1991) showed that the directional nonuniformities in the fracture surface are more important than the degree of surface roughness. Therefore Eq. (25) should be viewed as a simple fracture permeability tensor to approximate dense fracture networks with relatively smooth fracture surface. Note that the fracture permeability tensor is obtained by post processing the fracture network characteristics. We refer to Tuncay et al. (2000) for further details.

5. Illustrative basin simulations

5.1. Numerical simulation

The basin deformation model described in the previous sections was implemented in three dimensions using finite element techniques. Details on our approach are presented in the Appendix. Results presented below illustrate some of the many phenomena supported by this nonlinear basin dynamical system.

5.2. One-dimensional simulations

5.2.1. Comparison with an analytical solution

To verify our numerical approach, we compare predictions with an analytical solution obtained for the compaction of a viscoelastic layer overlying a rigid bed rock. The layer is subjective to its own weight. In the absence of fracturing and pressure solution, the total rate of strain tensor is $\underline{\underline{\dot{\epsilon}}}=\underline{\underline{\dot{\epsilon}}}^{pe}+\underline{\underline{\dot{\epsilon}}}^{vp}$ where $\underline{\underline{\dot{\epsilon}}}^{pe}$ and $\underline{\underline{\dot{\epsilon}}}^{vp}$ are given by Eqs. (2) and (9). To obtain the analytical solution we assume that elastic and viscous properties are constant and deformations are small. Letting z represent vertical distance measured from the surface (downward), the lateral stress, vertical stress and displacement are obtained in the form:

$$\sigma_{zz} = -\rho g z \tag{27}$$

$$\sigma_{yy} = -\frac{b}{b+c}\,\sigma_{zz} + \left(\frac{e}{d}+\frac{b}{b+c}\right)\sigma_{zz}\,\mathrm{e}^{-(b+c)(d-e)(2e+d)t/d}$$

$$w_3 = \frac{\rho g(h^2-z^2)}{2d}\left[\frac{(c+2b)(c-b)}{c+b}\,dt - \frac{2a^2}{(c+b)^2(d-e)(d+2e)}\,\mathrm{e}^{-(b+c)(d-e)(d+2e)t/d} + 1 + \frac{2a^2}{(c+b)^2(d-e)(d+2e)}\right]$$

where

$$a = ce + db + be \tag{28}$$

$$b = \frac{2\kappa + 2\mu/3}{(\kappa+4\mu/3)(2\kappa+2\mu/3)-2(\kappa-2\mu/3)^2}$$

$$c = \frac{\kappa-2\mu/3}{2\kappa+2\mu/3}\,b$$

$$d = \frac{(1-v)E}{(1+v)(1-2v)}$$

$$e = \frac{v}{1-v}\,d.$$

We take the model parameter values as $h=$ 0.5 km, Poisson's ratio $\nu=0.3$, elasticity modulus $e=10\,000$ MPa, $\kappa=\mu=10^{10}$ MPa s, $\rho=2200$ kg/m^3. The analytical and numerical results for the displacement w_3 of the surface as a function of time are illustrated in Fig. 3. The match between the analytical and numerical results is excellent.

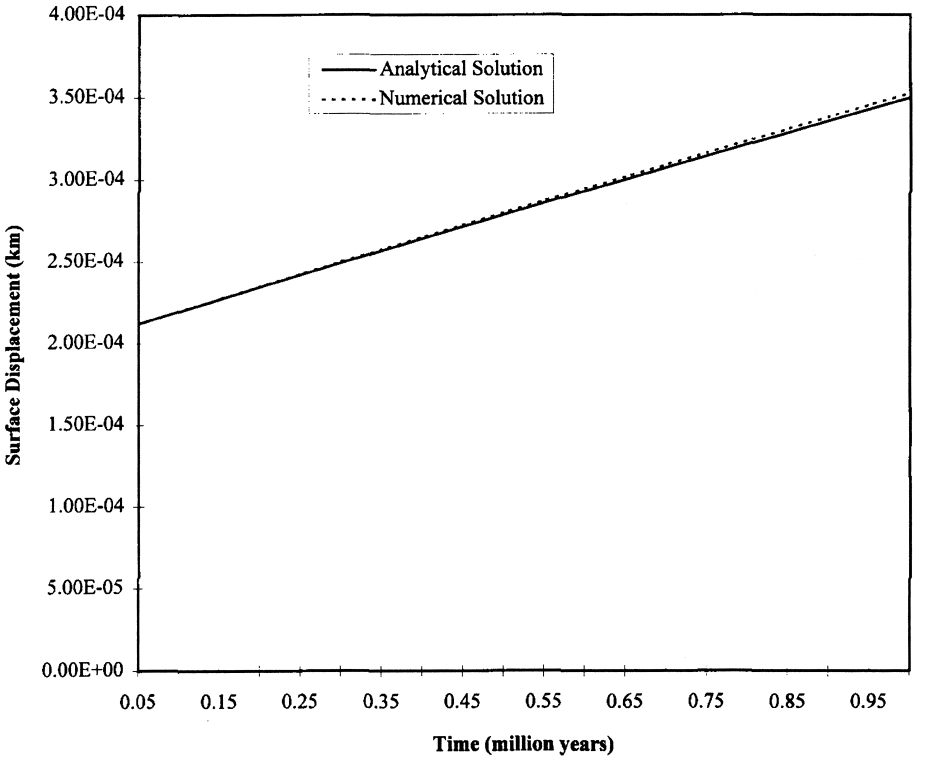

Fig. 3. Comparison of numerical and analytical results for the surface displacement.

5.2.2. Analytical solution for least compressive stress of a subsiding overpressured viscoelastic medium

An analytical solution is obtained for the least compressive stress of a subsiding, overpressured viscoelastic rock to illustrate some of the interesting aspects of our incremental stress approach. We assume that the vertical stress and pressure are given by:

$$\sigma_{zz} = \sigma^0_{zz} + A_3 t \tag{29}$$

$$P = P^0 + A_1 t + A_4 \cos(A_2 t)$$

where the superscript o refers to initial values, and the parameters A_i are constants. Then the lateral stress is obtained in the form:

$$\sigma_{zz} = (\sigma^0_{zz} - D_1 - D_3) \exp\left(- \frac{c_{11} + c_{12}}{d_{11} + d_{12}} t \right) + D_1 + D_2 t + D_3 \cos(A_2 t) + D_4 \sin(A_2 t) \tag{30}$$

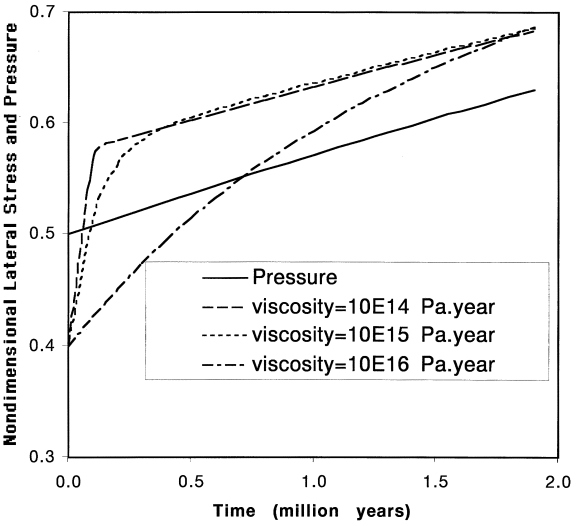

Fig. 4. History of lateral stress and pressure (Eqs. (29) and (11)). When the ratio of viscosities is kept constant ($R=1$), the lateral stress exceeds pressure in less than one million years even for high viscosities.

where

$$\sigma_{xx}^0 = -\frac{d_{12}}{d_{11}+d_{12}}(\sigma_{zz}^0+\alpha P^0)-\alpha P^0$$

$$d_{11} = (2K+2G/3)/[(K+4G/3)^2 + (K+4G/3)(K-2G/3)-2(K-2G/3)^2]$$

$$d_{12} = -\frac{K-2G/3}{2K+2G/3}\,d_{11}$$

$$c_{11} = (2\kappa+2\mu/3)/[(\kappa+4\mu/3)^2 + (\kappa+4\mu/3)(\kappa-2\mu/3)-2(\kappa-2\mu/3)^2]$$

$$c_{12} = \frac{\kappa+2\mu/3}{2\kappa+2\mu/3}\,c_{11}$$

$$Z = -(d_{11}+d_{12})^2 A_2^2 - (c_{11}+c_{12})^2$$

$$D_1 = [-(d_{11}+2d_{12})\alpha A_1 + (c_{11}+2c_{12})P^0 - d_{12}A_3 + c_{13}\sigma_{zz}^0 - (d_{11}+d_{12})D_2]/-(c_{11}+c_{12})$$

$$D_2 = [(c_{11}+2c_{12})A_1 + c_{12}A_3]/-(c_{11}+c_{12})$$

$$D_3 = [-(d_{11}+d_{12})(c_{11}+2c_{12})A_2A_4 + (d_{11}+2d_{12})(c_{11}+c_{12})\alpha A_2A_4]/Z$$

$$D_4 = [(d_{11}+2d_{12})(d_{11}+d_{12})\alpha A_2^2A_4 + (c_{11}+c_{12})(c_{11}+2c_{12})A_2]/Z.$$

In obtaining this result it was assumed that the material properties do not change in time, and deformations are small.

We take coefficients A_1, A_2, A_3, and A_4 as -0.1, 0, 0.05, and 0, respectively. The bulk and shear moduli are taken as $K=G=10$ GPa. In Fig. 4, the variation of pressure and lateral stress is shown for three different viscosities keeping the shear viscosity/bulk viscosity ratio R as one. As seen in the figure, depending on the magnitude of viscosity, the lateral stress eventually catches up to the fluid pressure. This rock will hardly fracture in a one-dimensional system unless there is a high rate of overpressuring such as from petroleum generation. Even for the high viscosity rock, the lateral stress reaches the fluid pressure in less than one million years.

The effect of the viscosity ratio R is illustrated in Fig. 5 where the coefficients A_i are taken as -0.1, 10, 0.05, and 0.1, respectively. In this figure, we keep the bulk viscosity as 10^{15} Pa year, and vary the shear viscosity of $R=0.5$ and $R=1$. For $R=0.5$, rock fractures at very high pressures whereas for $R=1$, rock fractures a number of times even at low pressures. This example shows that a simple criterion, such as assumption of fracturing when fluid pressure exceeds a certain fraction of lithostatic stress, is not valid for viscoelastic media.

The physics of stress evolution is complicated since bulk and shear viscosities are dictated by the evolving microscale rock texture. Concepts such as seals (low permeability zones) emerge but are tempered with notions of resistance to fracturing, i.e., should be of low R in character. In the next section, an example of episodic fracturing of a seal rock is illustrated.

5.2.3. Episodic oil ejection

As discussed in the previous section, most seal rocks will not fracture in a one-dimensional system (no geometric effects such as flexure) unless there is a high-rate, overpressuring mechanism in operation. In this section, we illustrated the effect of high rate of oil generation in a source rock just

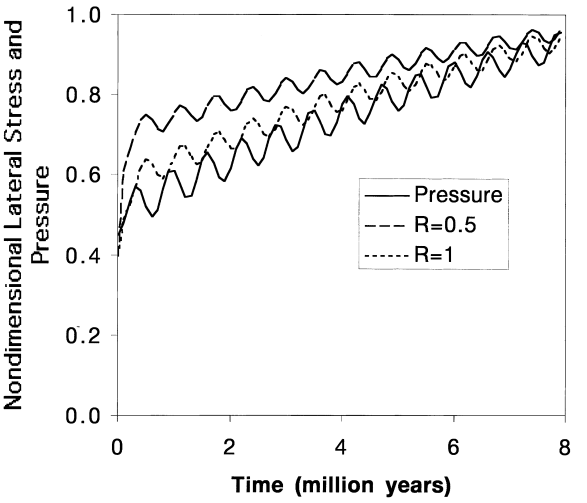

Fig. 5. History of lateral stress and pressure with harmonic pressure oscillation. For low viscosity ratio, lateral stress is higher than pressure except for very high, almost lithostatic stresses. When the viscosity ratio is high, pressure catches up with lateral stress a number of times.

below a seal. The location of the simulated system is the Andector Field of the West Texas Permian Basin (Tuncay et al., 1998). The basin is approximately 500 million years old. The history of sedimentation rate, and mineralogic and textural character are taken from published reports as are thermal and subsidence/upheaval, erosional and thermal (i.e., basement heat flux) histories (see Tuncay et al., 1998).

Evolution of overpressure at the bottom of the Ellenburger Formation is shown in Fig. 6. Overpressuring starts around 350 million years into the simulation when fractures in the layer above the source rock first disappear but then cyclically reappear. Oscillatory behaviour is a result of cyclic fracturing and healing of the seal (Fig. 7) driven by petroleum generation. After 470 million years, the cyclic petroleum expulsion ceases and the pressure, oil saturation, fracturing and other variables show a more steady behavior.

Fig. 7 illustrates the fracture permeability/depth profile time sequence demonstrating a fracture front moving through the seal located between 2450 and 2700 m. Overpressuring of the oil and water phases is primarily due to oil generation. It creates a fracture front that moves upward through the seal. Once the overpressure is released, the fractures close, which in turn results in descent of the fracture front and the recommencing of overpressuring. This cycle repeats until the oil generation rate slows down, or the seal remains fractured. The latter could occur due to an extremely high rate of petroleum generation or due to tectonic effects (flexure or overall extensional regime). Each fracture front cycle corresponds to one peak in Fig. 6 and to a pulse of oil release.

This type of overpressuring, fracturing, escape of fluids and the closure/healing of fractures (OFEC cycle) has been studied by a number of authors (Ghaith et al., 1990; Chen et al., 1994; Dewers and Ortoleva, 1995; Maxwell, 1997; see also discussion in Ortoleva, 1994a, 1998).

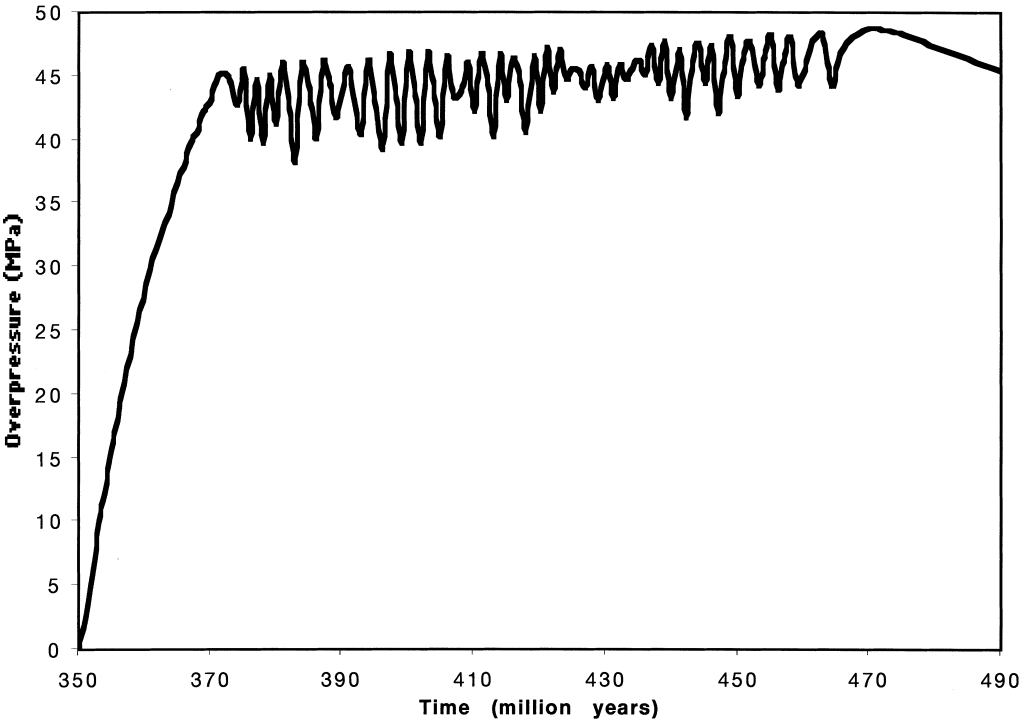

Fig. 6. Evolution of overpressure at the bottom of the Ellenburger Formation. Oscillatory behavior is a result of cyclic fracturing of the seal driven by petroleum generation.

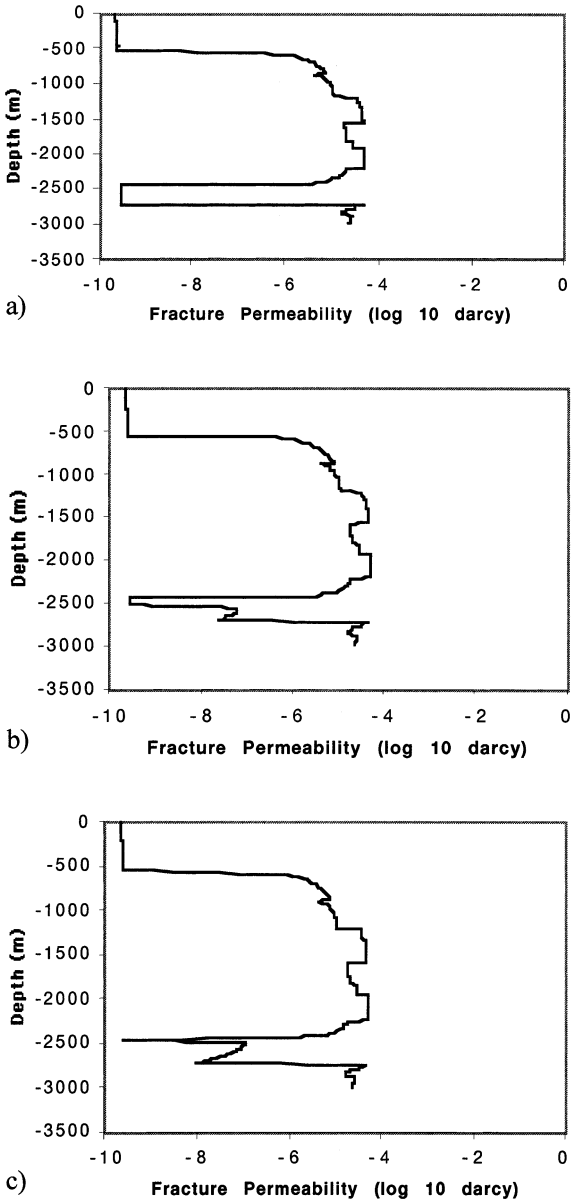

Fig. 7. Fracture permeability profile sequence illustrating the fracture front moving through the seal (between 2450 and 2700 m).

However, these studies of the OFEC cycle do not include the self-limiting character of fracturing as accounted for in the present incremental stress formulation. The present study shows that OFEC cyclicity can still occur and its characteristic of oscillator fracture front motion is still preserved.

5.3. Three-dimensional systems

5.3.1. Curvature versus permeability diagrams

A comprehensive RTM model derives its predictive power from its basis in the physical and chemical laws that govern the behavior of geological materials. This is in contrast to correlative approaches such as porosity/depth curves or curvature analysis that attempt to use statistical average behavior. Many aspects of geological systems involve a multiplicity of factors controlling their evolution and, furthermore, there are both memory-preserving and -destroying processes. Therefore, it does not seem that there are simple correlations between today's state variables and processes that operated tens or hundreds of million years ago. Here we examine such correlations within the framework of our basin model.

Fig. 8 shows a correlation diagram for permeability with local curvature. The data are taken from a simulation performed for the Piceance Basin, Colorado (see below). The curvature has been calculated as the sum of the absolute values of the curvature tensor $\kappa'_{it} \equiv \frac{1}{2}\{\partial n_i/\partial x_{i'} + \partial n_{i'}/\partial x_i\}$ where n_i is the upward pointing normal vector to the top of the lithologic layer in which the material point is located (at the closest point on the latter contact surface). This figure shows that prediction of fractured zones based on such a correlation is

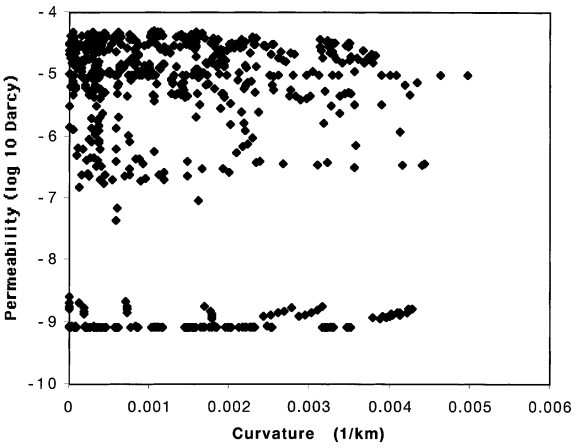

Fig. 8. Correlation of curvature with permeability shows little relation. The absolute sum of eigenvalues of the curvature tensor is used to represent curvature.

not a reliable approach. The correlation between curvature and fracturing is very weak. Indeed, fracturing is a very dynamic process, and is affected by many parameters such as fluid pressure, tectonic boundary conditions, rock viscosities and thermal regime as well as the time course of these factors.

To better understand this effort, the time course of the state of a particular material point in the permeability/curvature plane can be studied. Fig. 9 shows the complexity of such an evolution for two material points. The first material point shows a fast compaction period followed by fracturing and healing whereas the second material point shows compaction followed by fracturing. As today's rock state is only one point on such a trajectory, it is clear that there is little hope of finding a simple correlation for such a system. Fig. 9 shows the history of permeability and curvature for two material points (relatively brittle and ductile) as the basin evolves. First, the permeability reduces as a result of compaction. The brittle rock permeability and curvature correlates as the curvature increases during an early period. However, fractures remain open as the curvature disappears due to the changing tectonics. Following such trajectories leads one to strongly argue against the reliability of present-day (i.e., snapshot) correlations.

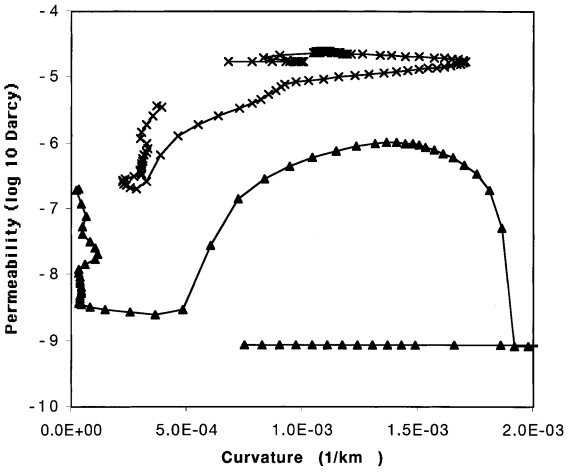

Fig. 9. Trajectory of a material point in the permeability/curvature plane. One of the material points heals whereas the other does not. The high permeability material point is in a sandstone layer.

5.3.2. Three-dimensional deformation of the south-central zone of the Piceance Basin

The map view of the simulation domain of this study is shown in Fig. 10. Data from five wells are used to reconstruct the sedimentation, erosion and subsidence/upheaval histories (shown in Fig. 10).

The Piceance Basin history and local site data were distilled into specific input files for the boundary conditions and initial data as follows. The depositional history input (thickness of units and ages of contacts) was constructed from well logs such that the sandstone to the mudstone ratio, as well as the total coal thickness in the Paludal Interval, are preserved. The sandstones in the Mesaverde Group were combined such that no single unit is less than 30 m thick, in order to satisfy the minimum thickness for the chosen resolution of the simulation grid. For simplicity, the overlying Wasatch Formation and younger units are left undifferentiated. Lithologic input (grain size distribution) for the Mesaverde Group was modified from petrographic data primarily for coarser grained units in the Mesaverde Group at the MWX site (Multiwell Experiment Project Groups at Sandia National Laboratories and CER Corporation, 1987, 1988, 1989, 1990). These data were compiled and averaged for sandstones in each interval in the Williams Fork Formation, and for each of the three major sandstone units in the Iles Formation. For the lithologic input of sandstone units, the sum of the observed average contents of quartz and feldspar minerals were assigned to the framework grains, and the observed total clay content was assigned to the clay matrix fraction. This composition is then normalized by the program to an assumed depositional porosity of 30%, based on average porosities for poorly to moderately sorted, very fine to medium grained, wet-packed sands (Beard and Weyl, 1973). Due to the paucity of available data for the composition of these mudstones and shales, the input compositions for this study are loosely based on general mudstone compositional data (Shaw and Weaver, 1965) and on compositional data of the Wasatch Formation mudstones (Hosterman and Dyni, 1972). These compositional fractions are then normalized in the program to account for an assumed depositional porosity of 25%. We refer to Payne

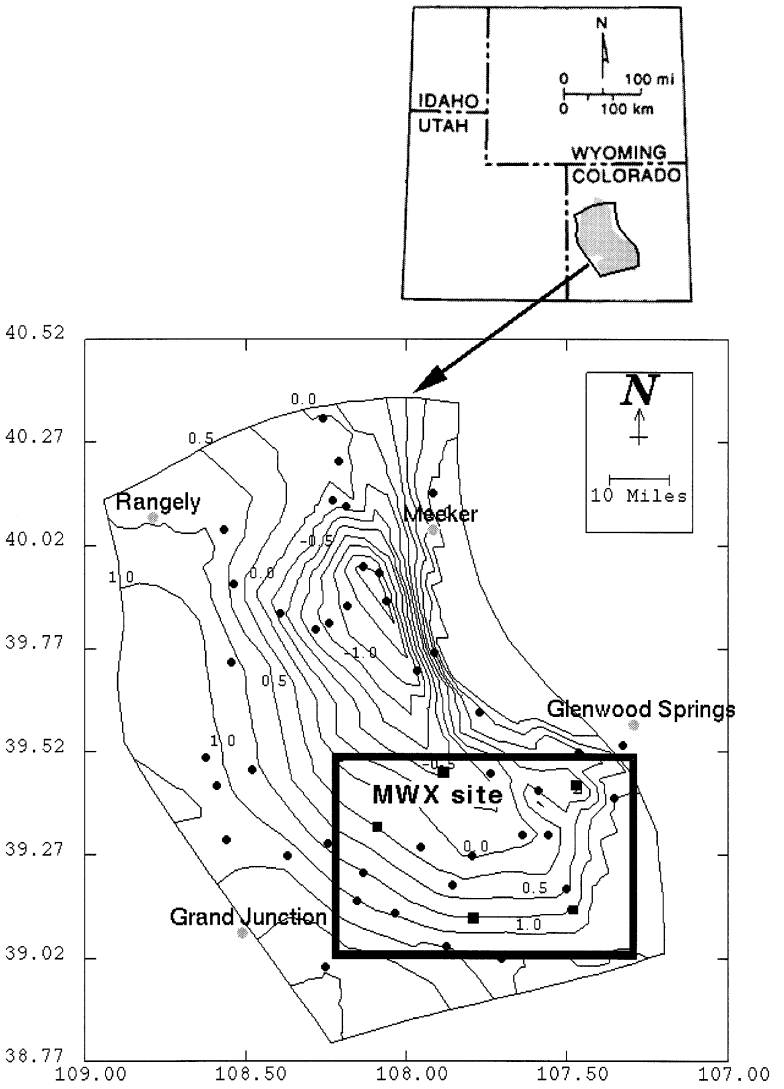

Fig. 10. Map view of the Piceance Basin and simulation domain (thick box). The small dots indicate locations of wells at which lithologic and other data are available whereas the square markers indicate locations of five wells used in the reconstruction of sedimentation and subsidence/upheaval histories.

et al. (2000) and Payne (1998) for further details on data preparation and the geologic history of the Piceance Basin.

Most of the natural gas production in the Piceance Basin is from fractured reservoirs. It is important to know the history of fracturing as well as the fractured zones today to understand the migration of petroleum from source rocks to reservoirs. Furthermore, it is interesting to delineate the complexity of such a three-dimensional fluid-rock system as an example of a dynamic crustal system. Thus, we simulate the 75 million year history of this basin.

The simulation starts with a flat and very thin (just a few hundred meters thick) computational domain. The subsidence rate is interpolated from the well data and used to impose a velocity of descent/upheaval at the bottom of the basin. Our

reconstructed sedimentation and erosion rate history are used to update the thickness of the uppermost layers of the sediment. When the thickness of the uppermost layer is greater than a specified value, the upper grid is split and thus the grid grows during deposition. During extended periods of erosion, the grid is automatically reorganized so as to maintain numerical stability and accuracy. The time dependent sea level is used to impose the normal traction at the top boundary of the sediment.

Fig. 11 shows the porosity distribution in a sandstone. During early times, the basin is quite flat and porosity–depth correlation, for a given lithology, is very strong. As the basin develops, the porosity distribution is strongly affected by the tectonic boundary conditions. In the last 10 million years of simulation, the curvature at the bottom decreases. However, the porosity distribution remains fairly complicated, illustrating the effect of the detailed history on the present day porosity distribution and the lack of a simple porosity–depth relationship.

Fig. 12 shows the isosurface of overpressure (15 bars) toned with depth. The back panel shows the permeability distribution. The structure of the folded, multiply layered surface is dictated by the interplay of lithological differences and fracturing, and shows the three-dimensional complexity of the continuity of overpressured zones. Thus, stacked overpressured compartments when viewed as a few pressure/depth curves yield little insight into the full three-dimensionality of the compartmentation structure.

A cross-sectional view of fracture length is shown in Fig. 13. The distribution of fracture length reflects lithologic variation and the topography imposed by the basement tectonics. The layered fracture length structure is closely related to the layering in the overpressure isosurface. While Figs. 12 and 13 illustrate the present day geometric complexity, further complexity is seen when these three-dimensional images are viewed in time sequence. These aspects of the deforming basin reflect its behavior as a nonlinear dynamical system. The layered nature of fracture zones shows the lithology dependence of fracturing, i.e., fractures in a brittle lithology discontinue at the interface of more ductile lithologies.

6. Conclusions

The challenge of basin modeling follows from the strongly coupled nature of the processes, the large number of operating processes and the fundamentally three-dimensionality of the problem. In the present study, an incremental stress formulation has been used to integrate the suite of basin RTM processes to understand basin deformation, fracturing, and stress history and the coevolving fluid, mineral and thermal systems. This coupled RTM system has been shown here to be capable of self-organizing compartments and oscillatory, episodic fluid flow. The present comprehensive basin modeling notion confirms that the basin is to be viewed as a self-organizing nonlinear dynamical system (Ortoleva et al., 1987a,b; Ortoleva, 1990, 1994a,b,c, 1998).

A key element of our approach is the coevolution of rock texture with macroscopic deformation. The introduction of dynamical texture variables into basin models started with the work in pressure solution where a model of grain size and shape was introduced to capture compaction, stylolites and diagenetic bedding (see Ortoleva, 1994a, 1994b for reviews). In these models, the texture $\Leftrightarrow$ deformation dynamic, models can be developed for phenomena heretofore not possible with decoupled or less comprehensive models.

Key challenges for the future of comprehensive, fully coupled, three-dimensional basin modeling are as follows:

- improve fracturing and faulting descriptions and rate laws;
- calibrate the RTM laws, notably those such as continuous irreversible deformation which operate on long time scales;
- develop more efficient numerical techniques and faster computer hardware (to attain the $>10^6$ finite element, >100 descriptive variables needed for truly comprehensive, spatially resolved simulations; and
- develop efficient methods for constructing the tectonic, thermal, and sedimentation histories directly from well logs, seismic or other "raw" data.

Calibration and validation of our model is an active research area in our laboratory at present.

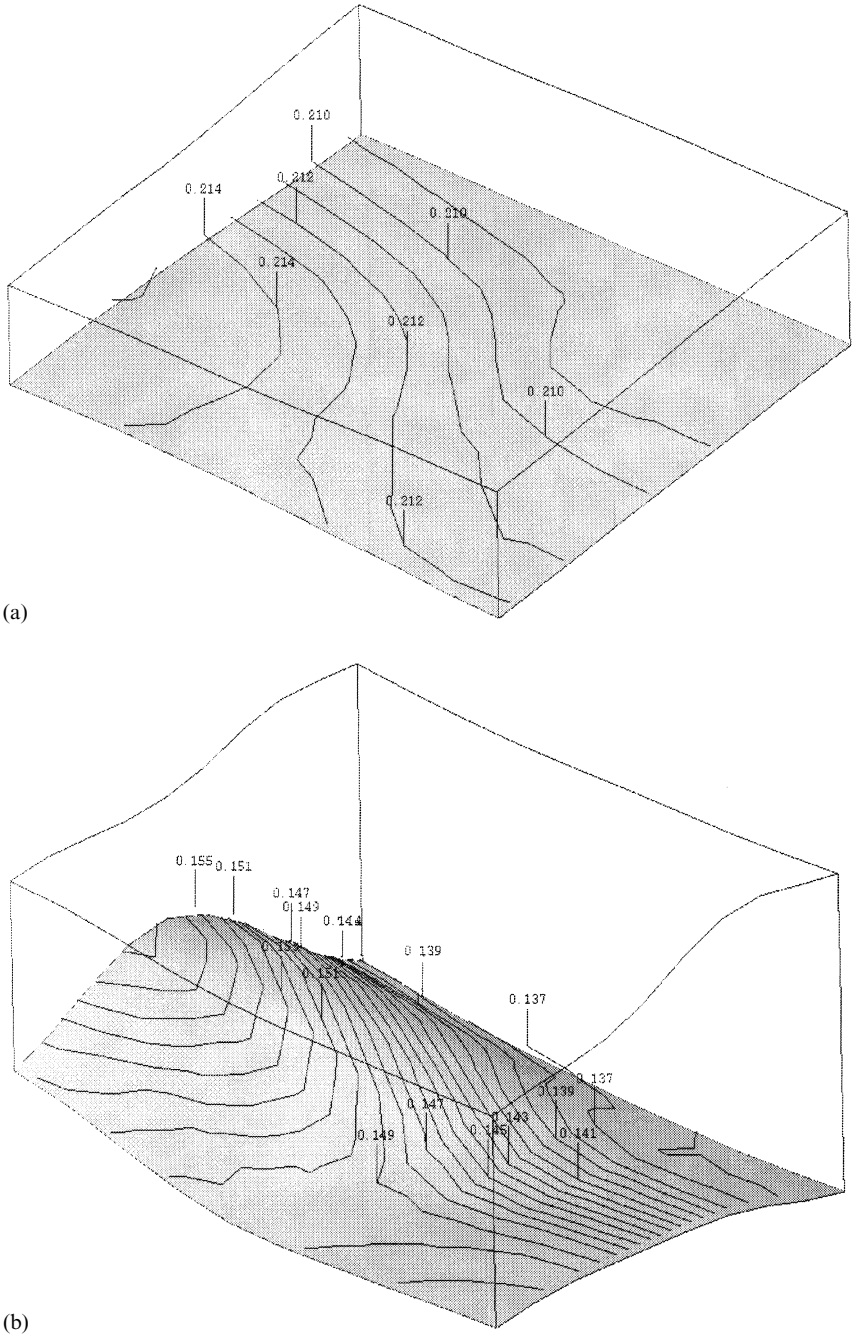

Fig. 11. Porosity contours at 20, 50 and 74 (present day) million years into the simulation.

Efforts are in two directions. Instantaneous relations such as permeability/textural laws, fracture growth laws, poroelastic coefficient formulae and diagenetic rate and equilibrium parameters are being calibrated by laboratory data. Very long time processes are not accessible to laboratory

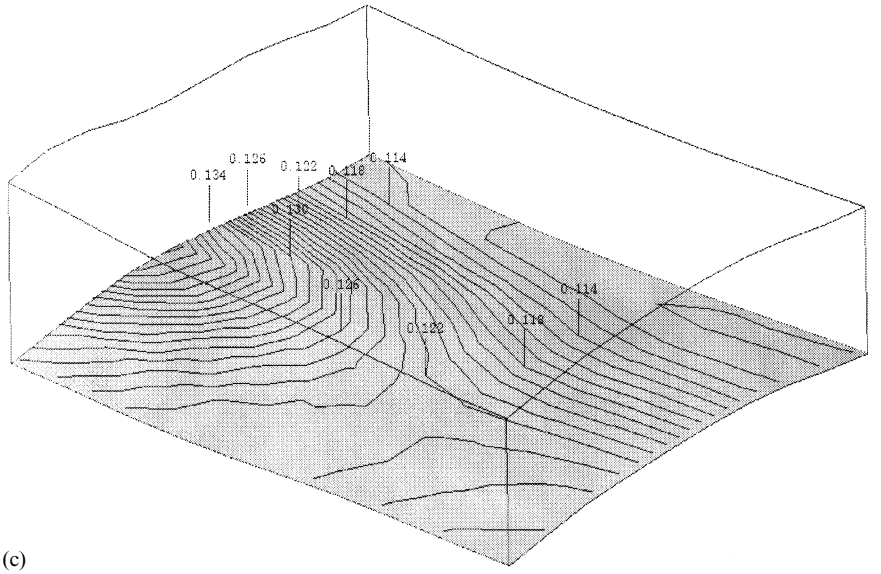

Fig. 11. (*continued*)

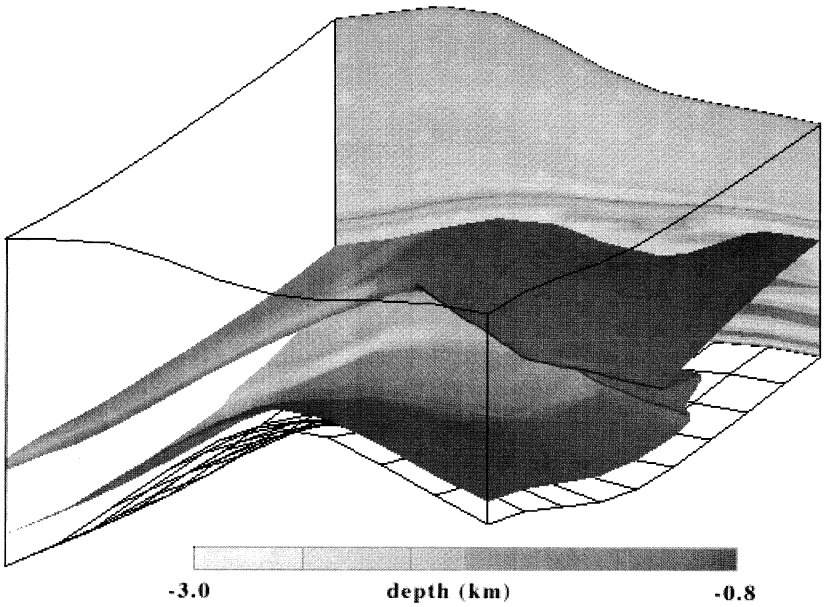

Fig. 12. Isosurface of 15 bars overpressure toned with depth. The cross-section at the back shows the permeability distribution. Different permeabilities reflect varying sediment compositions including porosity, texture and mineral grain sizes, and fractures.

experiments and are therefore being calibrated using geologic data. We have developed a "laboratory" basin database to fix these slow process parameters. This is not to be viewed as a correlation between overall basin properties and final basin state (such as porosity–depth curve, etc.) but rather is an approach to calibrating the physical and chemical parameters which are universal to

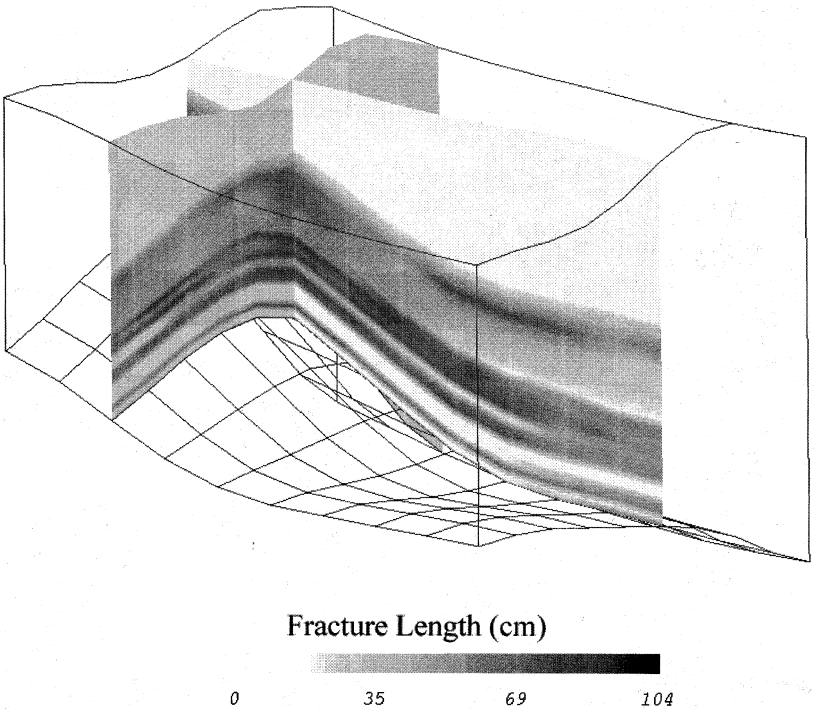

Fig. 13. Cross-sectional view of maximum fracture length illustrating the strong dependence of fracturing on lithology. Fractures discontinue at the interface of more ductile lithologies. Changing sediment properties, stress and fluid pressure during the evolution of the basin result in dynamic fracture patterns, which in turn significantly affect the anisotropy of fracture permeability. If the enhanced permeability from fracturing is significant, it can direct the flow of petroleum; understanding such occurrences of the past, therefore, can be important for identifying or understanding reservoirs in presently unlikely structural and stratigraphic locations.

all basins. With this laboratory and geological calibration approach we are also involved in validating our model on other basins not used in the calibration data set. We believe that this can be best achieved through collaborative efforts.

Our approach is of both fundamental and practical interest. Besides aiding in unraveling the dynamics of a basin, our results can be applied to:

- locating quality petroleum reservoirs;
- predicting properties of the earthquake cycle and fault dynamics in general;
- determining the mechanical stability of putative chemical waste storage reservoirs/compartments; and
- integrated management of basin water, mineral, petroleum, and related resources.

We believe that our extended incremental stress rheology provides the integration for the comprehensive, three-dimensional, RTM basin modeling needed to meet these fundamental and practical challenges.

Acknowledgements

This work has greatly benefited from conversations with and assistance from Ms. Spring Romer, Mr. Walid Sibo, Dr. Dorothy Payne and Dr. Gonca Ozkan. We thank Prof. J. Rice, Harvard University, for an introduction to the incremental stress concept. We also thank Xiaorong Luo and an anonymous reviewer whose suggestions improved the manuscript. This work was supported by a contract with the Gas Research Institute, the Office of Sciences of the U.S. Department of Energy, MEPTEC of Mobil Oil Company and Philips Petroleum Company.

Appendix: Numerical approach

In this study we use the updated Lagrangian approach to analyze the time dependent large deformation behavior of elasto-visco-plastic geological materials. In this approach, all static and kinematic variables are referred to an updated configuration in each time step. We first obtain the integral form of the momentum balance equation. We transform the integral form to a form which allows an incremental numerical procedure.

We consider the constitutive relations in the form of:

$$(\dot{\sigma}_{ij}+\alpha\dot{P}\delta_{ij})=D_{ijkl}(\dot{\epsilon}_{kl}-\dot{\epsilon}^{vp}_{kl}) \tag{A1}$$

where σ_{if} is the Cauchy (real) stress tensor (force per unit area in the deformed geometry), $\dot{\epsilon}_y$ is the rate of deformation tensor, D_{ijkl} is the fourth order elasticity tensor, a is the effective stress coefficient, and over dot denotes the material derivative. For the sake of simplicity we denote all deformation processes other than poroelasticity by $\dot{\epsilon}^{vp}_{if}$.

Displacement reformulation

It is convenient to reformulate the problem in terms of displacement defined for a small time step Δt. In that time, a material point at ${}^{t}\underline{x}$ moves to ${}^{t+\Delta t}\underline{x}$ through a displacement $\underline{w}$:

$${}^{t+\Delta t}\underline{x}={}^{t}\underline{x}+\underline{w} \tag{A2}$$

If $\underline{\sigma}$ changes continuously in time then we expect that:

$$\underline{w} \underset{\Delta t\to 0}{\sim} \Delta t\underline{v}. \tag{A3}$$

Thus for small Δt, $\underline{w}$ and $\underline{v}$ are equivalent. In what follows, the discretized time for mutation used will be for small Δt so that henceforth only deformation over a small time interval Δt will be discussed. Large scale deformation will be simulated as the accumulation of small displacements over many small Δt advancement steps.

The boundary conditions applied during the small time (Δt) period may be written as follows. Let S_ϕ and S_w be portions of the system boundary over which forces and displacements are specified, respectively. Then the boundary conditions to be imposed are:

$$w_i=w_i^S= \text{ on } S_w \text{ and } \sigma_{ij}n_j=t_i= \text{ on } S_\phi \tag{A4}$$

where t_i is the traction and w_i^s is the specified displacement. Eqs. (A1) and (II.5) form a set of nonlinear equations in terms of the stress tensor and deformation velocities. Since the deformations are large, the system constitutes a moving boundary problem.

Integral formation

To obtain the integral form, we multiply Eq. (II.5) by an arbitrarily chosen continuous displacements such as:

$$\delta w_i=0 \text{ on } S_w \tag{A5}$$

Then we integrate the equation over the total volume V:

$$\int_{t+\Delta t_V}({}^{t+\Delta t}\sigma_{ij,j}+{}^{t+\Delta t}f_i)\delta w_i dv=0 \tag{A6}$$

By using the divergence theorem, Eq. (A6) can be written as:

$$\int_{t+\Delta t_V}{}^{t+\Delta t}\sigma_{ij}\delta_{t+\Delta t}e_{ij}dv=\int_{t+\Delta t_V}{}^{t+\Delta t}f_i\delta w_i dv + \int_{t+\Delta t_S{}^{f}}{}^{t+\Delta t}t_i\delta w_i ds={}^{t+\Delta t}R \tag{A7}$$

where the left superscripts refer to the configuration of the body and the left subscripts refer to the coordinate axes, and e_y is the small strain tensor:

$${}_{t+\Delta t}e_{ij}=\tfrac{1}{2}({}_{t+\Delta t}w_{i,j}+{}_{t+\Delta t}w_{j,i}). \tag{A8}$$

Note that:

$$\delta_{t+\Delta t}e_{ij}=\delta\,\tfrac{1}{2}({}_{t+\Delta t}w_{i,j}+{}_{t+\Delta t}w_{j,i});\ {}_{t+\Delta t}w_{i,j}=\frac{\partial w_i}{\partial^{t+\Delta t}x_j} \tag{A9}$$

Incremental form

The solution of Eq. (A7) requires the location of the body at time $t+\Delta t$. Therefore we transform Eq. (A7) to the configuration at time t, by defining

the second Piola–Kirchoff stress ${}^{t+\Delta t}_{t}S_{ij}$ which refer to the stress at time $t+\Delta t$ but measured in the configuration at time t, as:

$$\int_{{}^{t}V} {}^{t+\Delta t}_{t}S_{ij}\delta {}^{t+\Delta t}_{t}l_{ij}dv = {}^{t+\Delta t}R \tag{A10}$$

where

$${}^{t+\Delta t}_{t}S_{ij} = \frac{{}^{t}\rho}{{}^{t+\Delta t}\rho}\left({}^{t}_{t+\Delta t}x_{i,s}\,{}^{t+\Delta t}\sigma^{t}_{sr\,t+\Delta t}\,{}^{t}_{t+\Delta t}x_{j,r}\right) \tag{A11}$$

$${}^{t+\Delta t}_{t}l_{ij} = \tfrac{1}{2}\left({}_{t}w_{i,j} + {}_{t}w_{j,i} + {}_{t}w_{k,i}\,{}_{t}w_{k,j}\right).$$

l_{if} is the Green–Lagrange strain tensor. Since the stresses and strains are unknown, the following incremental decompositions are used:

$${}^{t+\Delta t}_{t}S_{ij} = {}^{t}\sigma_{ij} + {}_{t}S_{ij} \tag{A12}$$

$${}^{t+\Delta t}_{t}l_{ij} = {}_{t}e_{ij} + {}_{t}\eta_{ij};\ {}_{t}e_{ij} = \tfrac{1}{2}\left({}_{t}w_{i,j} + {}_{t}w_{j,i}\right);$$

$${}_{t}\eta_{ij} = \tfrac{1}{2}{}_{t}w_{k,i}\,{}_{t}w_{k,j}$$

Substituting Eq. (A12) into Eq. (A10) yields:

$$\int_{{}^{t}V} {}_{t}S_{ij}\delta_{t}l_{ij}dv + \int_{{}^{t}V} {}^{t}\sigma_{ij}\delta_{t}\eta_{ij}dv = {}^{t+\Delta t}R - \int_{{}^{t}V} {}^{t}\sigma_{ij}\delta_{t}e_{ij}dv \tag{A13}$$

When the stress increment ${}_{t}S_{if}$ is given in terms of incremental displacements, Eq. (A13) becomes a nonlinear equation in terms of incremental displacements. It should be noted that Eqs. (A7) and (A13) are, theoretically, equivalent.

When the rate of deformation is small, Eq. (A1) can be written as:

$${}_{t}S_{ij} = D_{ijkl}({}_{t}e_{kl} - \Delta t\dot{\epsilon}^{vp}_{kl}) - \alpha\Delta t\dot{p}\delta_{ij} \tag{A14}$$

Finite element formulation

Eq. (A13) can be linearized as:

$$\int_{{}^{t}V} {}_{t}S_{ij}\delta_{t}e_{ij}dv + \int_{{}^{t}V} {}^{t}\sigma_{ij}\delta_{t}\eta_{ij}dv = {}^{t+\Delta t}R - \int_{{}^{t}V} {}^{t}\sigma_{ij}\delta_{t}e_{ij}dv. \tag{A15}$$

Substituting Eq. (A14) into Eq. (A15) yields:

$$\int_{{}^{t}V} D_{ijkl}\,{}_{t}e_{ij}\delta_{t}e_{ij}dv + \int_{{}^{t}V} {}^{t}\sigma_{ij}\delta_{t}\eta_{ij}dv = {}^{t+\Delta t}R - \int_{{}^{t}V} {}^{t}\sigma_{ij}\delta_{t}e_{ij}dv + \int_{{}^{t}V} (\Delta t D_{ijkl}\dot{\epsilon}^{vp} + \alpha\Delta t\dot{p}\delta_{ij})\delta_{t+\Delta t}e_{ij}dv \tag{A16}$$

When a standard formulation employing 8-node brick elements is used, approximating the displacement components in terms of its nodal values results in the following assembled matrix equation:

$$(K_L + K_{NL})\overline{w} = {}^{t+\Delta t}R - F - Z \tag{A17}$$

where

$$K^{e}_{L} = \int_{{}^{t}V^{e}} B^{T}_{L}DB_{L}dv \tag{A18}$$

$$K^{e}_{NL} = \int_{{}^{t}V^{e}} B^{T}_{NL}\,{}^{t}\sigma B_{NL}dv$$

$$F^{e} = \int_{{}^{t}V^{e}} B^{T}_{L}\hat{\sigma}dv$$

$$Z^{e} = \int_{{}^{t}V^{e}} B^{T}_{L}(\Delta t D\dot{\epsilon}^{\ vp} + \Delta t\alpha\dot{p})dv$$

$$K_L = \sum K^{e}_{L},\ K_{NL} = \sum K^{e}_{NL},\ F = \sum F^{e},\ Z = \sum Z^{e}$$

where the summation operator denotes the assemblage of the element matrices. In Eq. (A18) B_L, B_{NL}, D, $\hat{\sigma}$, ${}^{t}\sigma$ are the linear strain–displacement transformation matrix, nonlinear strain–displacement matrix, elasticity coefficients matrix, Cauchy stress matrix, and vector of Cauchy stresses in the configuration at time t, respectively. It is important to realize that Eq. (A16) is an approximation to the actual equation to be solved, Eq. (A13). Depending on the nonlinearities in the system, the linearization of Eq. (A13) may introduce errors. For this reason it may be necessary to iterate at

each time step until Eq. (A13) is satisfied to a required tolerance. The error is given by:

$$Error = {}^{t+\Delta t}R - \int_{t+\Delta t V} {}^{t+\Delta t}\sigma^{l}{}_{ij}\delta_{t+\Delta t}e^{l}{}_{ij}dv \qquad \text{(A19)}$$

where the superscript 1 refer to approximate values. We should note that the right-hand sides of Eqs. (A19) and (A16) are similar except the last integral arising from the visco-plastic strains.

Iteration procedure

Because of the inelastic effects, the solution is obtained in two steps. In the first step the nonlinear constitutive equations are solved for the incremental stresses. This requires the solution of six unknowns (components of stress tensor) at each selected point. We solve for the stress increments at the Gaussian points which results in an efficient integration of the integrals containing the stresses. If we use an implicit scheme, we can write:

$${}_{t}S^{m}_{ij} = D_{ijkl}({}_{t}e^{m-1}_{kl} - \Delta t({}^{t+\Delta t}\dot{\epsilon}^{vp}_{kl})^{m}) + \Delta t\dot{p}\delta_{ij} \qquad \text{(A20)}$$

where m is the iteration number. The incremental displacement can be solved from:

$$(K_L + K_{NL})\overline{w}^{m} = {}^{t+\Delta t}R - F^{m} - Z^{m} \qquad \text{(A21)}$$

We define the change in incremental displacement between iteration m and $m-1$ as:

$$\Delta\overline{w}^{m} = \overline{w}^{m} - \overline{w}^{m-1} \qquad \text{(A22)}$$

Substituting Eq. (A22) into Eq. (A21) yields:

$$(K_L + K_{NL})\Delta\overline{w}^{m} = {}^{t+\Delta t}R - F^{m} - Z^{m} - (K_L + K_{NL})\overline{w}^{m-1} \qquad \text{(A23)}$$

Eq. (A23) can be rewritten by considering Eqs. (A13), (A17) and (A19) as:

$$(K_L + K_{NL})\Delta\overline{w}^{m} = {}^{t+\Delta t}R - {}^{t+\Delta t}F^{m} \qquad \text{(A24)}$$

where

$${}^{t+\Delta t}F^{m} = \int_{t+\Delta t V^{m}} {}^{t+\Delta t}B^{m}_{L}{}^{t+\Delta t}\hat{\sigma}^{m}dv \qquad \text{(A25)}$$

The iteration continues until Δw becomes reasonably small. When the solution at $t+\Delta t$ is obtained, the Cauchy stress in the deformed configuration is obtained using the relations:

$${}^{t+\Delta t}_{t}S_{ij} = {}^{t}\sigma_{ij} + {}_{t}S_{ij} \qquad \text{(A26)}$$

$${}^{t+\Delta t}\sigma_{sr} = \frac{{}^{t+\Delta t}\rho}{{}^{t}\rho}{}_{t+\Delta T}{}_{t}x_{s,j}{}^{t+\Delta t}_{t}S_{ij}{}^{t+\Delta t}_{t}x_{r,j}. \qquad \text{(A27)}$$

This completes the iteration for $t = t+\Delta t$. Since the solution is obtained in two steps, our numerical scheme can also be applied to problems with different kinds of constitutive relations. In such cases, one needs to modify the first step (i.e., solution of incremental stress components). The second step remains unchanged since it is a conservation equation.

Once the incremental displacements are solved, porosity can be solved from the mass balance of solids assuming incompressible solid grains:

$$\frac{D\phi}{Dt} = (1-\phi)\underline{\nabla}\cdot\underline{u} \qquad \text{(A28)}$$

It should be noted that since the viscosities and elastic parameters depend on the state of stress, failure function, and porosity, they are updated at every iteration.

To optimize the convergence rate, we have introduced a dynamic relaxation parameter for Eq. (A22). This parameter automatically changes depending on the convergence rate. An observation of Eq. (A24) shows that as the right-hand side of Eq. (A24) approaches zero, the incremental displacement vanishes, i.e., solution is obtained. This can be achieved regardless of a rigorous stiffness matrix, which is nothing but a preconditioner of the system. Therefore, we only calculate the linear part of stiffness matrix whenever appreciable changes in the system are observed and used it as a conditioner for the displacements.

References

Bathe, K.J., 1996. Finite Element Procedures. Prentice Hall, Englewood Cliffs, NJ.

Bathe, K.J., Ramm, E., Wison, E.L., 1975. Finite element formulations for large deformation dynamic analysis. Int. J. Num. Meth. Eng. 9, 353–386.

Beard, D.C., Weyl, P.K., 1973. Influence of texture on porosity and permeability of unconsolidated sand. AAPG Bull. 57, 349–369.

Berkowitz, B., 1995. Analysis of fracture network connectivity using percolation theory. Math. Geol. 27, 467–483.

Berryman, J.G., 1980. Long-wavelength propagation in composite elastic media I: Spherical inclusions. J. Acoust. Soc. Am. 68, 1809–1819.

Berryman, J.G., 1986. Effective medium approximation for elastic constants of porous solids with microscopic heterogeneity. J. Appl. Phys. 69, 1136–1140.

Berryman, J.G., 1992. Single-scattering approximations for coefficients in Biot's equations of poroelasticity. J. Acoust. Soc. Am. 91, 551–571.

Biot, M.A., 1941. General theory of three-dimensional consolidation. J. Appl. Phys. 12, 155–164.

Biot, M.A., Willis, D.G., 1957. The elastic coefficients of the theory of consolidation. J. Appl. Mech. 24, 594–601.

Bour, O., Davy, P., 1998. On the connectivity of three-dimensional fault networks. Water Resource Res. 34, 2611–2622.

Chen, Y., Chen, W., Park, A., Ortoleva, P., 1994. In: Ortoleva, P. (Ed.), Role of pressure-sensitive reactions in seal formation and healing: Application of the CIRF A reaction-transport code. Basin compartments and seals AAPG Memoir No. 61. AAPG, Tulsa, Oklahoma, pp. 403–416.

Chen, M., Bai, M., Roegiers, J.-C., 1999. Permeability tensors of anisotropic fracture networks. Math. Geol. 31, 355–373.

Dewers, T., Ortoleva, P., 1990. Differentiated structures arising from mechano-chemical feedback in stressed rocks. Earth-Sci. Rev. 29, 283–298.

Dewers, T., Ortoleva, P., 1994. Nonlinear dynamical aspects of deep basin hydrology: fluid compartment formation and episodic fluid release. Am. J. Sci. 294, 713–755.

Druker-Prager, D.C., Prager, W., 1952. Soil mechanics and plastic analysis or limit design. Quart. Appl. Math. 10, 157–165.

Engelder, T., Geiser, P., 1980. On the use of regional joint sets as trajectories of paleostress fields during the development of the Appalachian Plateau New York. J. Geophys. Res. 85, 6319–6341.

Fischer, M.P., Gross, M.R., Engelder, T., Greenfield, R.J., 1995. Finite element analysis of the stress distribution around a pressurized crack in layered elastic medium-implications for the spacing of fluid-driven joints in bedded sediment-rock. Tectonophysics 247, 49–64.

Gassman, F., 1951. Uber die elastizität poröser medien. Vierteljahrsschrift der Naturforchenden Gesellschaft in Zürich 96, 1–23.

Ghaith, A., Chen, W., Ortoleva, P., 1990. Oscillatory methane release from shale source rock. Earth Sci. Rev. 29, 241–248.

Gross, M.R., 1993. The origin and spacing of cross joints – examples from the Monterey formation, Santa-Barbara coastline, California. J. Struct. Geol. 15, 737–751.

Haase, C.S., Chadam, J., Feinn, D., Ortoleva, P., 1980. Oscillatory zoning in plagioclase feldspar. Science 209, 272–274.

Hancock, P.L., Ali Kadhi, A., Walper, J.L., 1984. Regional joint sets in the Arabian platform as indicators of interplate processes. Tectonophysics 3, 27–43.

Harris, J.F., Taylor, G.L., Walper, J.L., 1960. Relation of deformational fractures in sedimentary rocks to regional and local structures. AAPG Bull. 44, 1853–1873.

Hosterman, J.W., Dyni, J.R., 1972. Clay mineralogy of the Green River Formation, Piceance Creek Basin, Colorado – A preliminary study. U.S. Geological Survey Professional 800, 159–163.

Kulander, B.R., Barton, C.C., Dean, S.L., 1979. The application of fractography to core and outcrop fracture investigations. U.S. Department of Energy, Morgantown Energy Technology Center Report METC/SP 79 (3), 174.

Larson, K.W., Waples, D.W., Fu, H., Kodama, K., 1993. Predicting tectonic fractures and fluid flow through fractures in basin modelling. In: Dore, A.G. (Ed.), Basin Modelling: Advances and Applications NPF Special Publications 3 Norwegian Petroleum Society. Elsevier, Amsterdam, pp. 373–383.

Lorenz, J.C., Teufel, L.W., Warpinski, N.R., 1991. Regional fractures I: A mechanism for the formation of regional fractures at depth in flat-lying reservoirs. AAPG Bull. 75, 1714–1737.

Luo, X., Vasseur, G., 1996. Geopressuring mechanism of organic matter cracking: numerical modeling. AAPG Bull. 80, 856–873.

Luo, X., Vasseur, G., Pouya, A., Lamoureux-Var, V., Poliakov, A., 1998. Elastoplastic deformation of porous medium applied to the modelling of compaction at basin scale. Mar. Petrol. Geol. 15, 145–162.

Mallory, W.W., 1977. Oil and gas from fractured shale reservoirs in Colorado and northwest New Mexico. Rocky Mountain Assoc. Geol. Spec. Publ. 1, 38.

Maubeuge, F., Lerche, I., 1993. A north Indonesian basin: geothermal and hydrocarbon generation histories. Mar. Petrol. Geol. 10, 231–245.

Maubeuge, F., Lerche, I., 1994. Geopressure evolution and hydrocarbon generation in a north Indonesian basin: two-dimensional quantitative modelling. Mar. Petrol. Geol. 104, 104–115.

Maxwell, J.M., 1997. The physical chemistry and nonlinear dynamics of compartment formation in sedimentary basins. Ph.D. Thesis, Indiana University, Bloomington.

Multiwell Experiment Project Groups at Sandia National Laboratories and CER Corporation, 1987. Multiwell Experiment Final Report: I. The Marine Interval of the Mesaverde Formation: Sandia National Laboratories Report, SAND87-0327.

Multiwell Experiment Project Groups at Sandia National Laboratories and CER Corporation, 1988. Multiwell Experiment Final Report II. The Paludal Interval of the Mesaverde Formation: Sandia National Laboratories Report, SAND88-1008.

Multiwell Experiment Project Groups at Sandia National

Laboratories and CER Corporation, 1988. Multiwell Experiment Final Report III. The Coastal Interval of the Mesaverde Formation: Sandia National Laboratories Report, SAND88-3284.

Multiwell Experiment Project Groups at Sandia National Laboratories and CER Corporation, 1988. Multiwell Experiment Final Report IV. The Fluvial Interval of the Mesaverde Formation: Sandia National Laboratories Report, SAND89-2612.

Nickelsen, R.P., Hough, V.N.D., 1967. Jointing in the Appalachian Plateau of Pennsylvania. Geol. Soc. Am. Bull. 78, 609–630.

Nicolis, G., Prigogine, I., 1977. Self-organization in non-equilibrium systems from dissipative structures to order through fluctuations. Wiley-Interscience, New York.

Nicolis, C., Nicolis, G., 1987. Irreversible phenomena and dynamical systems. Analysis in geosciences. D. Reidel Publishing Co., Dordrecht Holland.

Oda, M., 1985. Permeability tensor for discontinuous rock masses. Geotechnique 35, 483–495.

Oda, M., 1986. An equivalent continuum model for coupled stress and fluid flow analysis in jointed rock masses. Water Resources Res. 22, 1845–1856.

Oda, M., 1982. Fabric tensor for discontinuous geological materials. Soils and Foundations 22, 96–108.

Odling, N.E., 1992. Network properties of a two-dimensional natural fracture pattern. Pure Appl. Geophys. 138, 95–114.

Ortoleva, P., Hallet, B., McBirney, A., Meshri, I., Reeder, R., Williams, P., 1990. Self-organization in geological systems: Proceedings of a Workshop held 26–30 June. University of California at Santa Barbara Earth Sci. Rev. 29, 1–3.

Ortoleva, P., 1979. The multifaceted family of the nonlinear waves and fields center dynamics, catastrophes rock bands and precipitation patterns. In: Pacault, A., Vidal, C. (Eds.), Synergetics Far From Equilibrium. Springer-Verlag, New York, pp. 114–127.

Ortoleva, P., 1990. Self-organisation in Geological Systems Special Issue, Ortoleva, P. (Ed.), Earth Sci. Rev. Spec. Publ. 29.

Ortoleva, P., 1993. Self-organization and nonlinear dynamics in sedimentary basins. Phil. Trans. Roy. Soc. Lond. 344, 171–179.

Ortoleva, P., 1994a. Geochemical Self-organization. Oxford University Press, New York.

Ortoleva, P. (Ed.), 1994b. Basin Compartments and Seals, AAPG Memoir No. 61, AAPG, Tulsa, Oklahoma.

Ortoleva, P., 1994c. Development of diagenetic differentiated structure through reaction-transport feedback. In: Wolf, K.H., Chilingarian, G.V. (Eds.), in: Diagenesis 4, 39–52.

Ortoleva, P., Merino, E., Chadam, J., Moore, C.H., 1987a. Geochemical self-organization I: Reaction-transport feedback mechanisms and modeling approach. Am. J. Sci. 287, 979–1007.

Ortoleva, P., Merino, E., Moore, C.H., Chadam, J., 1987b. Geochemical self-organization II: The reactive-infiltration instability. Am. J. Sci. 287, 1008–1040.

Ortoleva, P., 1998. Basin compartments and seals. Report prepared for the Gas Research Institute, No. GRI-97/0097.

Ozkan, G., Ortoleva, P., 1999a. Mechanical failure of cavities in poroelastic media. Submitted for publication.

Ozkan, G., Ortoleva, P., 1999b. Evolution of gouge grain size distribution: a Markov model. Submitted for publication.

Ozkan, G., Tuncay, K., Ortoleva, P., 1998. Process-based fault seal/conduit prediction,. 1998 AAPG Annual Convention Abstracts (CD-ROM format) May 17–28. AAPG, Salt Lake City, UT.

Payne, D., 1998. A new, fully coupled, reaction–transport––mechanical approach to modeling the evolution of methane reservoirs in the Piceance Basin. Ph.D. diss., Indiana University, Bloomington, IN.

Payne, D., Tuncay, K., Park, A., Comer, J., Ortoleva, P., 2000. Role of gas generation in natural fracture development and compartmentation in the Piceance Basin. AAPG Bull. (in press).

Renard, F., Ortoleva, P., Gratier, J.P., 1997. Pressure solution in sandstone: influence of clays and dependence on temperature and stress. Tectonophysics 280, 257–266.

Renard, F., Park, A., Ortoleva, P., Gratier, J.P., 1999. A transitional pressure solution model. Tectonophysics. (in press).

Rice, J.R., 1975. Continuum mechanics and thermodynamics of plasticity in relation to microscale deformation mechanisms. In: Argon, A.S. (Ed.), Constitutive Equations in Plasticity. MIT Press, Cambridge, MA, pp. 23–79.

Roberts, S.J., Nunn, J.A., 1995. Episodic fluid expulsion from geopressured sediments. Mar. Petrol. Geol. 12, 195–204.

Schneider, F., Potdevin, J.L., Wolf, S., Faille, I., 1996. Mechanical and chemical compaction model for sedimentary basin simulators. Tectonophysics 263, 307–317.

Segall, P., Pollard, D.D., 1983. Joint formation in granitic rock of the Sierra Nevada. Geol. Soc. Am. 94, 563–575.

Shaw, D.B., Weaver, C.E., 1965. The mineralogical composition of shales. J. Sed. Petrol. 35, 213–222.

Sonnenthal, E., Ortoleva, P., 1994.

Synder, M.D., Bathe, K.J., 1981. A solution procedure for thermo-elastic-plastic and creep problems. Nucl. Eng. Design 64, 49–80.

Thomson, M.E., Brown, S.R., 1991. The effect of anisotropic surface roughness on flow and transport in fractures. J. Geophys. Res. 96, 21923–21932.

Tuncay, K., Park, A., Ozkan, G., Zhan, X., Hoak, T., Sundberg, K., Ortoleva, P., 1998. Predicting the natural state of fractured carbonate reservoirs: Andector Field West Texas test of a 3-D RTM simulator. Paper in DOE/SAIC Final Report prepared for Contract DE-AC22-94PC91008.

Tuncay, K., Park, A., Ortoleva, P., 2000. A forward model of three dimensional fracture orientation and characteristics. J. Geophys. Res. (in press).

Turcote, D.L., 1992. Fractals, chaos, self-organized criticality and tectonics. Terra Nova 4, 4–12.

Ungerer, P., Burrus, J., Doligez, B., Chenet, P.Y., Bessis, F., 1990. Basin evaluation by integrated two-dimensional modeling of heat transfer, fluid flow, hydrocarbon generation and migration. AAPG Bull. 74, 309–335.

Waite, M.E., Ge, S., Spetzler, H., Bahr, D.B., 1998. The effect of surface geometry on fracture permeability: A case study using a sinusoidal fracture. Geophys. Res. Lett. 25, 813–816.

Wang, C., Xie, X., 1998. Hydrofracturing and episodic fluid flow in shale-rich basins – a numerical study. AAPG Bull. 82, 1857–1869.

Wu, H.Q., Pollard, D.D., 1995. An experimental study of the relationship between joint spacing and layer thickness. J. Struct. Geol. 17, 887–905.

Zienkiewicz, O.C., Cormeau, I.C., 1974. Visco-plasticity and creep in elastic solids – a unified numerical solution approach. Int. J. Num. Meth. Eng. 8, 821–845.